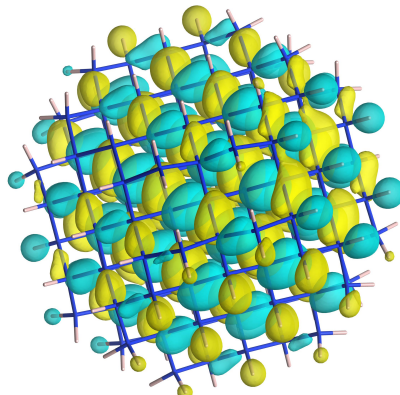

Theoretical investigation of surface functionalized silicon quantum dots

What effect does the attachment of organic ligands with aromatic compounds have on silicon quantum dots?

Report Bachelor Project Physics and Astronomy, size 15 EC, conducted between
30-03-2020 and 15-07-2020



AUTHOR	Mario van Rooij
STUDENT NUMBER	11607521
INSTITUTE	Van der Waals-Zeeman Institute
NAME OF FACULTY AND UNIVERSITY	Faculty of Science / University of Amsterdam
DATE OF SUBMISSION	04-08-2020
DAILY SUPERVISOR	Morice Corentin
SUPERVISOR	Katerina Dohnalova
SECOND EXAMINER	Jasper van Wezel

Abstract

Quantum dots (QDs) are nanometer-scale crystals that have contrasting properties to their bulk variants, which is especially true for indirect bandgap materials. Besides the size of the material, we can also modify the surface coverage of the QDs. After an introduction in the theoretical framework of density functional theory, we will present the effect of surface coverage of a silicon QD with organic molecules as found by density functional theory. We find that the radiative rates of the silicon QD increase significantly after adding organic ligands to the surface as compared to the hydrogen covered QD. Furthermore, we find a charge transfer between the ligand and the core upon certain excitations.

Samenvatting

Kwantumstippen zijn kleine varianten van kristallen (op de nanometer schaal) die zich anders gedragen dan grote kristallen. Specifiek gaat het hier om silicium kwantumstippen. In dit onderzoek zullen we eerst bespreken hoe dit soort structuren theoretisch onderzocht kunnen worden. Daarna zullen we kijken wat er gebeurt wanneer we de waterstofatomen op het oppervlak van de kwantumtip vervangen met organische moleculen. Uit dit onderzoek blijkt dat het toevoegen van dit soort moleculen aan het oppervlak een groot effect heeft op hoe effectief de kwantumtip licht uitstraalt.

Contents

1	Introduction	5
2	Quantum Dots	5
2.1	Definition	5
2.2	Production And Application	5
2.3	Silicon QD Properties	6
2.4	Silicon QDs With Ligands	6
2.4.1	Interesting ligands	6
3	Density Functional Theory	7
3.1	Schrödinger Picture Of The Many-Body Problem	7
3.2	Hohenberg-Kohn Theorems	8
3.3	Kohn-Sham Equations	9
3.4	Exchange Correlation Functional	10
3.4.1	Hartree Density Functional Approximation	10
3.4.2	Local Density Approximation	10
3.4.3	(Meta) Generalized Gradient Approximation	11
3.4.4	Hybrid (Meta) Functionals	11
3.5	Pseudo-Potentials	11
3.6	Basis Sets	11
3.6.1	Plane waves	12
3.6.2	Atomic orbitals	12
3.6.3	Gaussian plane waves	13
4	Time-Dependent Density Functional Theory	13
4.1	Runge-Gross Theorem	14
4.2	Van Leeuwen Theorem	14
4.3	Time Dependent Kohn-Sham Equations	14
4.4	Linear response theory and excitation energies	14
4.4.1	Absorption and emission spectra	15
5	Methods	15
5.1	HOMO- And LUMO-States	16
5.2	Band Structures	17
5.3	Isosurface Plots Of Orbitals	18
5.4	Energy-Level Diagrams	19
5.5	Thermalized Radiative Rate	19
5.6	TDDFT	23
5.6.1	Excitation Energy	24
6	Pyrene Functionalized QD	24
6.1	HOMO- LUMO-State	24
6.2	Charge Transfer	24
6.3	Comparison To Hydrogen Capped QD	24
6.4	Comparison Of DFT And TDDFT	26
6.5	Comparison To Experiment	29

7 Discussion And Outlook	31
8 Conclusion	31
9 Acknowledgments	31
A Installing CP2K On Linux	32
A.1 Installation	32
A.2 Execution	32
B Supporting information	33
B.1 Supporting Graphs	33
B.2 Shape Of Realistic QDs	33

1 Introduction

Silicon LEDs, lasers, and photovoltaics have been a goal for mankind for a long time because silicon is very abundant (about 28% of the Earth's crust by mass [1]) and non-toxic. Unfortunately, this is not possible due to the indirect bandgap of silicon, which makes it emit and absorb poorly. Making silicon devices more efficient or finding new silicon devices can have profound and unforeseen impacts on our society. In the field of photovoltaics, there have been several strategies to improve device performance. One of those techniques is to reshape the spectrum of the incoming sunlight. This means that we convert the energy that is radiated at a certain wavelength to another wavelength. This is useful because some devices (and organisms) can use some wavelengths more efficiently than others. A theoretical investigation may reveal mechanisms that play an important role in such reshaping. This, in turn, may reveal what structures could be used to most efficiently reshape the solar spectrum, potentially improving or finding new technologies that use this feature. We approach the simulation of silicon QDs with the tools of density functional theory, which is an *ab initio* theory, meaning that it is solely funded on hypotheses and involves no input from physical measurement. Further exploration of surface functionalization of silicon QDs could lead to samples that are even more radiative and hence practically applicable in medical, agricultural, or photovoltaic fields.

2 Quantum Dots

2.1 Definition

In bulk crystals, electrons have three spatial dimensions to move in. In quantum wells and wires, this dimensionality is reduced to 2 and 1 dimension(s), respectively. The next logical step is to confine the electron in all three directions. This is what we call a **quantum dot** (QD). At which length scale do we say the “dimensionality” is gone? The interesting phenomena occur at the 10 – 100 Å range when the radius is comparable or smaller than the excitonic Bohr radius (the distance between electron and hole in a bulk excitation). This is the so-called “quantum confinement regime” and this is where we draw the line. These structures typically consist of tens to thousands of atoms.

QD structures can be tuned to exhibit behavior that can be used in novel nano-optoelectronics. Optical, vibrational, and electronic properties of the crystal change tremendously when the crystal is small enough. Applying external perturbations to QDs, such as covering the surface with molecules or applying strain, can also influence their characteristics [2]. Besides all of this, the emission wavelength of the QD can be tuned by adjusting the size, shape, and structure.

2.2 Production And Application

The field of QD synthesis is a relatively new one. The first monodisperse (having the same size) QDs were synthesized around the year 1990, although this was delayed for Si. The monodispersion was essential to distinguish the effect of the size on the QDs. QD production methods can be divided into “bottom-up” and “top-down” routes. Colloidal synthesis of QDs is the most common bottom-up method of creation. A specific example of this technique goes along these lines [3]:

1. Some precursor of a semiconductor is injected.

2. The QDs form and properties can be influenced by heating time and other factors.
3. A surfactant is dissolved into a liquid and the mixture is heated. This surfactant has the function of passivizing the QDs.

This route is not very successful with silicon because of its distinctly different, covalent chemistry. The colloidal synthesis routes for Si QDs are highly underdeveloped and mostly practiced and successful so far are the plasma synthesis [4] and sol-gel synthesis [5].

Typical top-down techniques obtain QDs from larger structures, such as electrochemical etching [6] or milling of bulk crystals [7].

Fluorescent QDs have found applications in LEDs, displays [8], solar cells, spectral shapers for photovoltaics, and medical applications such as biomarkers [9, 10].

2.3 Silicon QD Properties

Silicon QDs (Si QDs) have picked up a lot of attention in the last decade. Silicon is abundant, non-toxic, and has covalent bonding, which can result in stable structures. This makes Si QDs a suitable candidate for medical applications such as drug delivery, sensors, and bio-imaging [11]. LEDs using Si QDs have also been proposed, but perform significantly worse than regular LEDs [12]. Compared to bulk silicon the radiative rate of Si QDs can increase by 3-4 orders of magnitude [9], which is usually observed in indirect bandgap semiconductor QDs. This, combined with the right surface coverage, can give Si QDs almost direct bandgap-like properties [13]. Additionally, covalently attached ligands can, in theory, be used for straining of the core, which can additionally modify the transition rates [14].

2.4 Silicon QDs With Ligands

One particular modification of the silicon QD that has been investigated extensively experimentally is the addition of an organic ligand to the QD [15, 16, 17, 18, 19, 20]. By doing this, the Si QDs display different behavior than without these ligands. One such behavior is an energy transfer from ligand to the QD [21]. The practical application of this mechanism has already been achieved in crop harvesting, where coated silicon QDs stimulated the growth of lettuce [22]. The potential application of this energy transfer mechanism is the conversion of solar energy from one wavelength to another. This would be done by attaching a ligand that absorbs a certain wavelength and transfers the absorbed energy to the silicon QD core, where it is re-emitted at another wavelength. Most organic molecules absorb in the UV part of the spectrum and a Si QD can be tuned to emit over a wide range of wavelengths [9]. This method can enhance certain solar panels and crops which are more efficient in the longer wavelength regime by effectively reshaping the incoming solar spectrum. The mechanisms of this energy transfer have not yet been completely revealed and a density functional theory study has the potential to reveal some of the features at play.

2.4.1 Interesting ligands

In one study, the authors looked at the effect of surface coating the Si QDs with ligands that displayed a possible energy transfer. In this study, the sample was excited using a wavelength that is absorbed by the ligand. The interesting aspect is that this excitation energy is not re-emitted by the ligand, but transferred to the Si QD core, which then emits the light, effectively quenching the ligand and enhancing the core emission [23].

Three interesting ligands used in this study were pyrene, perylene, and phenanthrene. These ligands all show a potential energy transfer from ligand to the core upon absorbance of the right wavelength. This energy transfer is likely to be caused by a Förster Resonance Energy Transfer (FRET). For the FRET to work a donor and acceptor are needed where the emission spectrum of the donor has to overlap with the excitation spectrum of the acceptor. FRET can happen between QDs of different sizes, but also between a ligand and a QD [24]. If FRET is present, the donor fluorescence and exciton lifetime decrease while the acceptor fluorescence and exciton lifetime increase. This was observed in QDs functionalized with pyrene [23] and 1-(allyloxymethyl)pyrene [18]. For other structures that were alike, there was a splitting of the lifetime or even an increase in the lifetime.

3 Density Functional Theory

Density functional theory (DFT) provides a quantum mechanical framework in which electronical properties of materials can be predicted accurately. DFT is a first principle theory, meaning that no adjustable parameters are needed to calculate properties. By using this theory, one can simulate materials before production in so-called “reverse engineering”, which saves a tremendous amount of effort, especially with hard to produce Si QDs [25]. DFT was first introduced by Hohenberg & Kohn in 1964 [26]. For his contribution, Kohn was awarded the Nobel prize in 1998. The basic idea is to reduce the original $3(N+M)$ -dimensional many-body Schrödinger equation, where N is the number of the electrons in the system and M is the number of nuclei, to an $N \times 3$ -dimensional problem. This is done by implementing the Born-Oppenheimer approximation and introducing the electron density $n(\mathbf{r}) = \langle \Psi | \hat{n}(\mathbf{r}) | \Psi \rangle$, which yields information about the observables of the system and is the central quantity of DFT.

3.1 Schrödinger Picture Of The Many-Body Problem

In the exact treatment of the many-body problem, such as solid materials or molecules, the behavior of electrons and nuclei is governed by the Schrödinger equation (here for simplicity we assume time-independent case for static potentials):

$$\hat{H}\Psi(\mathbf{r}_1, \dots, \mathbf{r}_N, \mathbf{R}_1, \dots, \mathbf{R}_M) = E_{tot}\Psi(\mathbf{r}_1, \dots, \mathbf{r}_N, \mathbf{R}_1, \dots, \mathbf{R}_M), \quad (1)$$

where \mathbf{r}_i is the location of the i -th electron, \mathbf{R}_i is the location of to the i -th nucleus, E_{tot} is the total energy of the system and \hat{H} is the corresponding Hamiltonian operator.

Equation 1 is almost always simplified using the Born-Oppenheimer approximation, which reflects the fact that the movements of electrons, which are light compared to the cores, have an only negligible effect on the movement of the nuclei, or in other words, the timescale of the electronic motion is small compared to the movement of the nuclei. This allows for separation of the wavefunction into a nuclear and an electronic part:

$$\Psi(\mathbf{r}_1, \dots, \mathbf{r}_N, \mathbf{R}_1, \dots, \mathbf{R}_M) = \Psi_e(\mathbf{r}_1, \dots, \mathbf{r}_N)\Psi_n(\mathbf{R}_1, \dots, \mathbf{R}_M). \quad (2)$$

The e and n subscripts indicate the electronic and nuclear wavefunction, respectively. This separation allows us to solve the electronic and nucleonic parts separately by splitting the Schrödinger equation to independent nucleonic and electronic parts. The nucleonic part of the Hamiltonian contains the kinetic energy of the nuclei (often neglected) and Coulombic

repulsion between the different nuclei, giving constant energy E_{nuc} that can later be added to the electronic total energy. The electronic part is the part treated by DFT and is described by a Hamiltonian (shown in atomic units):

$$\hat{H} = [\hat{T} + \hat{V}_{e-e} + \hat{V}_{e-n}] = \sum_i \left(-\frac{1}{2} \nabla_i^2 \right) + \frac{1}{2} \sum_{i \neq j} \frac{1}{|\mathbf{r}_i - \mathbf{r}_j|} + \sum_{i,A} \frac{-Z_A}{|\mathbf{r}_i - \mathbf{R}_A|}, \quad (3)$$

with \hat{T} being the operator for the kinetic energy of electrons, \hat{V}_{e-e} being the interaction between the electrons and \hat{V}_{e-n} being the interaction between the electrons and (static) nuclei, also called the external potential V_{ext} .

Even with this simplification, equation 1 is often unsolvable or incredibly hard to solve.

Luckily, Walter Kohn has suggested a relatively simple solution, which uses the concept of electron density. The DFT method stands on two main pillars - “Hohenberg-Kohn theorems” 1 and 2 and uses a self-consistent iterative way to solve the so-called Kohn-Sham equations, which are the Schrödinger equation formulated in terms of electron density.

3.2 Hohenberg-Kohn Theorems

To find the ground state energy and electron density, we first have to formulate the Kohn-Sham equations. The first Hohenberg-Kohn theorem states (and proves) that there is a one-to-one correspondence between the external potential and the ground-state electron density. This means that every observable (such as ground state energy) can be written as a unique functional of the density, i.e.

$$\langle O \rangle = \langle \Psi | \hat{O} | \Psi \rangle = O[n] \quad (4)$$

The specific operator that returns the energy is the Hamiltonian, which for a system of electrons is defined by equation 3. Using the Hamiltonian, one can calculate the total energy of the system:

$$E[n(\mathbf{r})] = \langle \Psi[n(\mathbf{r})] | \hat{H} | \Psi[n(\mathbf{r})] \rangle, \quad (5)$$

which together with the fact that the wavefunction is a functional of the electron density leads to the expression for the energy:

$$E[n] = \hat{T}[n] + \hat{V}_{e-e}[n] + \hat{V}_{ext}[n] \quad (6)$$

This term is often rewritten by separating the terms. The kinetic term $T[n]$ is split into a term of a non-interacting system, $T_0[n]$, and a correlation term $T_c[n]$. The electron-electron interaction term $V_{e-e}[n]$ is split into the direct coulombic interaction term called Hartree energy $E_H[n]$ and the quantum mechanical exchange term $E_x[n]$. The correlation and exchange terms are joined in the so called “exchange-correlation” term $E_{xc}[n]$. At this point, we can also add the constant contribution from the repulsion between nuclei $E_{nuc} = \frac{1}{2} \sum_{I \neq J} \frac{Z_I Z_J}{|\mathbf{R}_I - \mathbf{R}_J|} = \text{const.}$ This results in the following functional for the energy:

$$E[n] = T_0[n] + E_H[n] + E_{xc}[n] + E_{ext}[n] + E_{nuc} \quad (7)$$

From these terms only the exchange-correlation function $E_{xc}[n]$ is unknown, and if its exact form was found, this treatment would lead to the exact solution. Finding approximations for

the exchange-correlation functional that are computationally feasible and accurate, however, is a complex research field by itself.

Next, to obtain the ground-state electron density we consider the second Hohenberg Kohn theorem, which utilizes the variational principle. This states that the lowest energy is obtained by calculating the energy functional with the ground state many-electron wavefunction and thus the ground-state electron density:

$$\Psi_0 = \Psi_0[n_0] \quad (8)$$

and

$$E[n] \geq E[n_0] \quad (9)$$

This means that the next problem that arises is the calculation of the ground state electron density n_0 , which in DFT treated in a self-consistent iterative way. Hence the ground-state electron density has to obey the following variational equation with constraints:

$$\frac{\delta \{E[n] - \mu \{ \int n(\mathbf{r}) d\mathbf{r} - N \} \}}{\delta n(\mathbf{r})} = 0, \quad (10)$$

where E is the total energy of the electronic system, N is the number of electrons, $n(\mathbf{r})$ is the electron density and μ is a Lagrange multiplier. The constraints $\int n(r) dr = N$ ensures that the system is normalized to the correct number of electrons N .

After obtaining an appropriate approximation for the ground state energy as a functional of the electron density and ensuring the normalization to N electrons with a Lagrange multiplier, one obtains the following equation:

$$E[n] = T_0[n] + E_H[n] + E_{xc}[n] + E_{ext}[n] + E_{nuc} - \mu \{ \int n d\mathbf{r} - N \}. \quad (11)$$

One can now apply the functional derivative and this becomes [27]:

$$\frac{\delta E[n]}{\delta n} = \frac{\delta T_0[n]}{\delta n} + v_{ks}(\mathbf{r}) - \mu, \quad (12)$$

where v_{ks} is called the Kohn-Sham potential and equals:

$$v_{ks} = \frac{\delta E_H[n]}{\delta n} + \frac{\delta E_{ext}[n]}{\delta n} + \frac{\delta E_{xc}[n]}{\delta n} \quad (13)$$

The variational principle states that this functional derivative should have a stationary value for the the ground state electron density, resulting in the equation:

$$\frac{\delta T_0[n]}{\delta n(\mathbf{r})} + v_{ks}(\mathbf{r}) = \mu. \quad (14)$$

3.3 Kohn-Sham Equations

One can now recognize that equation 12 is the same for a system of N independent particles [26] “living” in the potential:

$$V_{eff}(\mathbf{r}) = v_{ks}(\mathbf{r}). \quad (15)$$

This key insight allows us to calculate the ground state electron density for an interacting system by using an auxiliary non-interacting system. This leads to an independent set of N equations for single electron-like quasi-particles, called the Kohn-Sham equations (here in atomic units):

$$\left[-\frac{1}{2} \nabla^2 + V_{\text{eff}}(\mathbf{r}) \right] \psi_i(\mathbf{r}) = \epsilon_i \psi_i(\mathbf{r}), \quad (16)$$

The individual wavefunctions have no proof of being physical although the exact Kohn-Sham equations can approximate the optical gap to within a small error [28]. However, the complete set of Kohn-Sham equations does yield the ground state electron density of the system since it obeys the same equation:

$$n(\mathbf{r}) = \sum_{i=1}^N |\psi_i(\mathbf{r})|^2 \quad (17)$$

These equations are solved numerically in a self-consistent, iterative way because the effective potential depends on the wavefunctions themselves.

3.4 Exchange Correlation Functional

The sophistication with which the exact exchange-correlation functional is approximated varies widely. The approximations are often summarized in "Jacob's Ladder" [29]. The ranking in this ladder from worst to best is:

1. Hartree theory
2. Local density approximation (LDA)
3. (Meta) Generalized gradient approximation (GGA, meta GGA)
4. Hybrid (meta) generalized gradient approximation (Hybrid GGA and Hybrid meta GGA)
5. Fully non-local functionals

From these approximations, only the first 4 will be discussed because they are the relevant approximations for this project.

3.4.1 Hartree Density Functional Approximation

The worst approximation is often called "Hartree's Earth". In this approximation, the exchange-correlation functional is set to zero. The difference from the original Hartree-Fock approximation is that it does not take into account the non-local interaction and thus it performs worse. The Hartree-Fock theory, on the other hand, is more expensive computationally, scaling by a factor N^4 instead of N^3 with the size of the basis set used [30].

3.4.2 Local Density Approximation

This approximation assumes that the exchange-correlation potential at a point is only dependent on the value of the electron density at that point. One of the first approximations of this fashion was derived by Dirac in 1930 [31] in which he calculated the exchange-correlation term for a homogeneous electron gas analytically. This term was then assumed to work for non-homogeneous systems as well, which can be achieved by dividing the system in cubes of $d^3 \mathbf{r}$.

3.4.3 (Meta) Generalized Gradient Approximation

The generalized gradient approximation takes into account that the system is not homogeneous. This results in terms that are dependent on the derivative of the electron density at each point in space, in addition to the LDA. There are multiple ways in which approximations of this kind are derived, but the two main ways were by numerical fitting and basic principles derived from quantum mechanics. Another class of approximations that have arisen are the meta generalized gradient approximations, which take into account higher-order derivatives of the electron density.

3.4.4 Hybrid (Meta) Functionals

Hybrid functionals are a mix of the generalized gradient approximation and the Hartree-Fock approximation. The percentage is chosen to fit experiments. Hybrid meta functionals are another set of hybrid functionals that start from a meta generalized gradient approximation and mix this with a percentage of Hartree-Fock exchange-correlation.

3.5 Pseudo-Potentials

One approximation that is made to solve the Kohn-Sham equations is to split up the atoms into two categories - the core electrons and the valence electrons. This has a physical and practical reason.

The justification for this lies in the fact that the radial density of the core electrons is high near the core and the radial density of the valence electrons peaks at a greater distance from the core. Since the valence electrons are often of the order of bonding length [32], it can be assumed these are the electrons that participate most in bonding and so core electron interactions can be ignored in specific calculations.

The core electrons density is then simplified in such a way that it still correctly reflects the true electron density but has a smoother character, i.e we filter out the fast oscillating features of the orbitals near the nuclei. This effective electron density is then accompanied by the respective smooth effective potential.

Practically, in such a computation, only the valence electron energies are available as the solutions to the KS-equations, resulting in a significant reduction in the computational time.

There are many different types of pseudo-potentials, some including relativistic effects that can be relevant e.g. heavy atoms. Of course, the pseudo-potential is different for every different atomic specie.

3.6 Basis Sets

Quantum mechanical problems can be formulated in the so-called Schrödinger wave(function) formalism or in the Heisenberg's matrix formulation. The latter approach is preferred for use in numerical simulations, such as DFT.

To do this, we choose a complete set of basis functions to solve the Kohn-Sham equations given by equations 16. The original wavefunction can be expressed as a linear combination of the basis set functions:

$$\phi_v(\mathbf{r}) = \sum_i c_i^v \chi_i(\mathbf{r}), \quad (18)$$

with coefficient i running through all the basis set functions. Substitution of this linear expansion of the wavefunction in equation 16, and taking the inner product with $\chi_{i'}^*(\mathbf{r})$, leads to the secular equation:

$$\sum_{i'}(H_{ii'} - \epsilon_v S_{ii'})\mathbf{c}_i^v = 0, \quad (19)$$

where \mathbf{c}_i^v is a column vector and the matrix elements in $H_{ii'}$ and $S_{ii'}$ are defined as:

$$H_{ii'} \equiv \int \chi_i^*(\mathbf{r}) h_{ks} \chi_{i'}(\mathbf{r}) d\mathbf{r}$$

$$S_{ii'} \equiv \int \chi_i^*(\mathbf{r}) \chi_{i'}(\mathbf{r}) d\mathbf{r},$$

with h_{ks} being the one-particle Hamiltonian and $S_{ii'}$ the overlap integral, which is zero for orthogonal basis functions. Equation 19 can now be solved to obtain the eigenvectors and eigenvalues, i.e. the solutions for energies and orbitals of the Kohn-Sham equations.

Different DFT codes often choose one of the different types of basis - typically based either on plane waves or atomic orbitals. In the next sections, these will be discussed in more detail.

3.6.1 Plane waves

Commonly used in computational solid state physics is the “plane wave method”. Here the Kohn-Sham orbitals are expressed in the plane-wave basis, which is the solution to the free particle problem:

$$\phi_i(\mathbf{r}) = \frac{1}{\Omega} \sum_{\mathbf{G}} c_i \exp\{i\mathbf{G} \cdot \mathbf{r}\}, \quad (20)$$

Where G are the reciprocal lattice vectors and Ω is the unit cell volume. To capture the fine features of the electronic density, one needs to use plane waves with large G , which increases the basis set and hampers the computational effectiveness. Therefore, we typically set a cutoff energy which defines the accuracy of the calculation:

$$E_{cut} = \frac{1}{2} |G_{max}|^2. \quad (21)$$

Substituting equation 20, one can now find the eigenvectors and eigenvalues using numerical methods to solve for the coefficients.

The advantage of this method is that it is independent of the type and positions of the atoms in the system and the only parameter that needs to be chosen/adjusted is the cut-off energy. Also, the overlap integral $S_{ii'}$ is a unit matrix (orthogonality is fulfilled). Furthermore, this method allows for the advantageous use of the fast Fourier transforms (FFT) algorithms and periodic boundary conditions, where for the aperiodic systems, such as molecules, periodicity is achieved by repeating the supercell.

3.6.2 Atomic orbitals

More intuitive and often used in chemistry are the atomic orbital basis sets. These are hydrogen-like orbital functions:

$$\phi_i(\mathbf{r}) = \sum_{nlm} c_{nlm} R_{nl}(r) Y_{lm}(\phi, \theta), \quad (22)$$

Where $c_{I,nlm}$ are the unknown coefficients, R_n and Y_{lm} are the radial and spherical solution to the atomic Schrödinger equation, respectively and n , l and m are the relevant quantum numbers.

The radial part is often approximated by a Gaussian function:

$$R_{nl} \propto r^n \exp\{-\alpha r^2\}. \quad (23)$$

This method can greatly increase the speed of the calculations because we need a much smaller number of basis functions, and hence the diagonalization of the matrix 19 is computationally fast [33]. However, such a basis set is not orthogonal, hence $S_{ii'}$ is not a unity matrix, but usually a sparse matrix, thanks to the small overlap between the Gaussians.

To optimize the precision, for the radial part, a combination of several Gaussians is typically used for each orbital (so-called “double-zeta” or “triple-zeta” basis sets, or contracted basis sets). For the angular part, we usually add so-called polarization functions, which are functions with the higher angular momentum functions (e.g. p-function added to the atom with only s-function orbitals, etc.), which allows capturing angular distortions better.

3.6.3 Gaussian plane waves

In the DFT code cp2k, used in this project, a dual basis set is used, combining advantages of the two basis set approaches - the Gaussian and plane waves method (GPW) in a so-called “Quickstep” [34].

In this dual basis, electronic density can firstly be represented in Gaussians as

$$n(\mathbf{r}) = \sum_{ij} P^{ij} \phi_i(\mathbf{r}) \phi_j(\mathbf{r}), \quad (24)$$

where P^{ij} is density matrix and $\phi_v(\mathbf{r}) = \sum_i d_{iv} g_i(\mathbf{r})$ with $g_i(\mathbf{r})$ being the Gaussian basis set functions. The second (plane waves) representation gives:

$$\tilde{n}(\mathbf{r}) = \frac{1}{\Omega} \sum_{\mathbf{G}} \tilde{n}(\mathbf{G}) \exp(i\mathbf{G} \cdot \mathbf{r}). \quad (25)$$

This approach allows us to evaluate some parts of the Kohn-Sham equation on a real space grid (everything except the Hartree energy) and some parts in the reciprocal space (Hartree energy). This has the advantage that the computation method scales linearly with the number of electrons $\mathcal{O}(N)$. This is because (i) for the Gaussian part - we can assume so-called “screening”, i.e. most overlap terms S_{ij} are almost zero, thanks to the fact that Gaussians overlap very little if the centers are far enough; and (ii) for the plane waves part - we can use Fast Fourier Transforms to compute the Hartree energy [34].

4 Time-Dependent Density Functional Theory

To describe time-dependent phenomena, a time-dependent density functional theory (TDDFT) is required. The proof of such a method requires a Hohenberg-Kohn theorem that is time-dependent. Theorems were proven for restricted systems [35], but it was not until 1983 that Runge and Gross proposed a theorem for more general systems [36]. Another essential theorem to time-dependent density functional theory is the van Leeuwen theorem, which was proposed in 1999 [37] and proved that the time-dependent electron density could be reproduced by a non-interacting system.

4.1 Runge-Gross Theorem

The Runge-Gross theorem states that two time-dependent densities that evolve from the same initial many-electron wavefunction Ψ_0 , $n(\mathbf{r}, t)$ and $n'(\mathbf{r}, t)$ will develop into different electronic densities after an infinitesimal time step dt in a potential if those potentials differ by more than a time dependent constant (since this does not add any force):

$$v'(\mathbf{r}, t) \neq v'(\mathbf{r}, t) + c(t). \quad (26)$$

This means that there is a one-to-one correspondence between an electronic density and potential for a given initial many-electron wavefunction.

4.2 Van Leeuwen Theorem

The van Leeuwen theorem states that the electron density $n(\mathbf{r}, t)$ for a many body system with an interaction term $w(\mathbf{r}_1, \mathbf{r}_2)$, external potential $v(\mathbf{r}, t)$ and initial state Ψ_0 , there is a different system with an interaction term $w'(\mathbf{r}_1, \mathbf{r}_2)$ and a unique potential $v'(\mathbf{r}, t)$ that produces the exact same electronic density. The initial state has to be chosen such that at the electronic density and the time derivative are the same at the initial time.

The Runge-Gross theorem is a special case of this for $w'(\mathbf{r}_1, \mathbf{r}_2) = w(\mathbf{r}_1, \mathbf{r}_2)$. It follows from the theorem that $n(\mathbf{r}, t)$ is unique for a given potential $v(\mathbf{r}, t)$.

The case that is useful to produce a time-dependent Kohn-Sham theory is the one where $w'(\mathbf{r}_1, \mathbf{r}_2) = 0$. In this case, the van Leeuwen theorem says that there is some unique potential $v(\mathbf{r}, t)$ that reproduces the electron density of the real system. This case has been encountered before in the Kohn-Sham section. The problem that arises this time is to find the time-dependent potential that reproduces the density of the real system.

4.3 Time Dependent Kohn-Sham Equations

The most useful application of TDDFT is on systems that are initially in a ground state and encounter a perturbation from some time t_0 . Because of the Kohn-Sham theorem, the initial wavefunctions of the interacting and non-interacting systems are unique functionals of the ground state electron density. The strategy here is to solve the time independent KS equations first, which lead to an initial density. Then, at a time t_0 , the time dependent potential influences the system and the KS orbitals follow the following equation:

$$\left[-\frac{1}{2} \nabla^2 + v_s(\mathbf{r}, t) \right] \psi_i(\mathbf{r}, t) = i \frac{\partial}{\partial t} \psi_i(\mathbf{r}, t), \quad (27)$$

where $v_s(\mathbf{r}, t)$ is the time dependent KS potential. The initial state is obtained from the time independent theory and is then time propagated by equation 27.

4.4 Linear response theory and excitation energies

Linear response theory is used to directly calculate small perturbations in density caused by time-dependent perturbations. This can be applied in e.g. interaction of the system with weak optical fields. This saves a lot of computational time compared to calculating the complete time-dependent Kohn-Sham scheme. The strategy to calculate excitation energies is to look at the density-response function of a system. This function is a measure for change in the electron density when the system experiences a certain perturbation and diverges for a perturbation

that excites the system. The exact details of this method are beyond the scope of this thesis, but the theory will be used to obtain excitation energies.

4.4.1 Absorption and emission spectra

The absorption spectrum of a substance is a measure for how well the substance absorbs light of a given energy $E = h\nu$. Absorption can occur, if there is an available transition $E = E_{ij} = E_j - E_i$ between a populated state E_i and empty state $E_j > E_i$. Such transition will have a certain rate, given by Einstein's coefficient (in atomic units):

$$B_{ij} = f_{ij}/E_{ij}, \quad (28)$$

where f_{ij} is the oscillator strength, which is calculated as:

$$f_{ji} = \frac{2}{3}E_{ji}|<j|\hat{r}|i>|^2. \quad (29)$$

Emission is the reverse process, where the excited carrier from state E_j relaxes into a lower energy level E_i by the emission of a photon of energy $E = E_{ij}$. The rate of emission is given by the Einstein coefficient (in atomic units):

$$A_{ji} = 2E_{ji}^2 f_{ji}/c^3. \quad (30)$$

This is also what we call the radiative rate between two states (k_{rad}^{ji}), which is an indication of how likely a transition between two states is when the system is electromagnetically perturbed by an energy of around E_{ij} .

The linear response TDDFT gives us an approximation for the excited state energies and the oscillator strengths. However, the output are precisely defined "delta-function-like" energies, while in reality, every transition energy is broadened due to the Heisenberg relations of uncertainty between energy and time by $\Delta E \approx \hbar A_{ji}$. The linewidth is then described by Lorentzian profile [38]:

$$\varphi(E) \propto \frac{1}{1+x^2}, \quad (31)$$

with $x = 2\frac{E-E_{ji}}{A_{ji}}$.

Further Lorentzian or Gaussian line broadening can occur as a result of collisions and thermal motion, respectively, but these are neglected in our calculations for simplicity. A common practice is to broaden the delta peaks obtained with TDDFT with a standard deviation of 200 meV [39] in order to make the spectrum comparable to experimental data.

5 Methods

The crystals were designed with crystal editor freeware *Vesta* [40] and surface ligands were added using molecular editor freeware *Avogadro* [41]. The structure is defined by Cartesian coordinates of its atoms in the .xyz type of file. To obtain the relevant properties of the structure, there are two (or three) steps:

1. The geometry of the structure needs to be relaxed, in other words, we have to find the geometry with the lowest total energy by moving the atoms around. This is equivalent to finding the minimum of the potential energy surface for the atoms.

Sample	HOMO-LUMO Gap (eV)	Comparison study [45] (eV)
Si-5	6.02	5.75
Si-10	5.30	4.71
Si-29	3.84	3.58
Si-35	3.69	3.58
Si-47	3.29	3.50

Table 1: Comparison of our simulation results of different silicon QD samples compared to results of [45].

2. The ground state orbitals and energies have to be found in order to calculate properties such as the HOMO-LUMO gap, radiative rate, or a band structure.
3. To obtain excited states and oscillator strengths more precisely, we perform TDDFT calculation on the ground state optimized structure.

The simulations were all done using the “Quickstep” method in the CP2k [34]. We used the double-zeta MOLOPT basis set with d -like polarization functions, adapted to large size systems [42], and energy cut-off of 400 Ry for the plane waves. The pseudo-potentials that were used are the Goedecker, Teter, and Hutter (GTH) pseudo-potentials [43]. As an exchange-correlation functional, we used GGA functional PBE [44].

To test our DFT calculations, we ran test simulations on nanocrystals which previously have been investigated in literature [45, 46, 47], simulated in different DFT codes with different settings. We compared both spherical and cubic QDs. The resulting energies of these simulations are depicted in Figure 1. Our results showed a slight overestimation of the HOMO-LUMO gap compared to most other studies (For the comparison with the study in ref. [45], see the Table. 1), but showed the same general trend, where larger samples had a smaller HOMO-LUMO energy gap.

The case where our HOMO-LUMO gap was smaller than the comparison study can be explained by the fact that in [46] a more sophisticated exchange-correlation function was used. Degoli et al. [45] used a GGA PBE functional and [47] used a LDA functional. The fact that our HOMO-LUMO gap lies between study [45] and [46] makes sense. This is caused by the difference in precision between the two methods. It is not possible to say which approximation (LDA or GGA) performs better for these SiQDs, since their performances differ per system, but often the LDA neglects extra interaction from the surrounding electron density resulting in a net underestimation as compared to generalized gradient methods. The study using the PBE functional [45] used plane waves which yield similar underestimation, compared to the Quickstep method which utilizes both Gaussian orbitals and plane waves.

5.1 HOMO- And LUMO-States

HOMO (highest occupied molecular orbital) and LUMO (lowest unoccupied molecular orbital) states play an important role in solid-state physics because they approximate the bandgap of a material.

The HOMO-state is defined such that it is the orbital with the highest energy that is occupied in the system at zero temperature. Opposed to it is the LUMO state, which is the state that has the lowest energy compared to all other unoccupied states and is unoccupied. Since electrons (or holes) can only make discrete steps in energy when excited, the difference

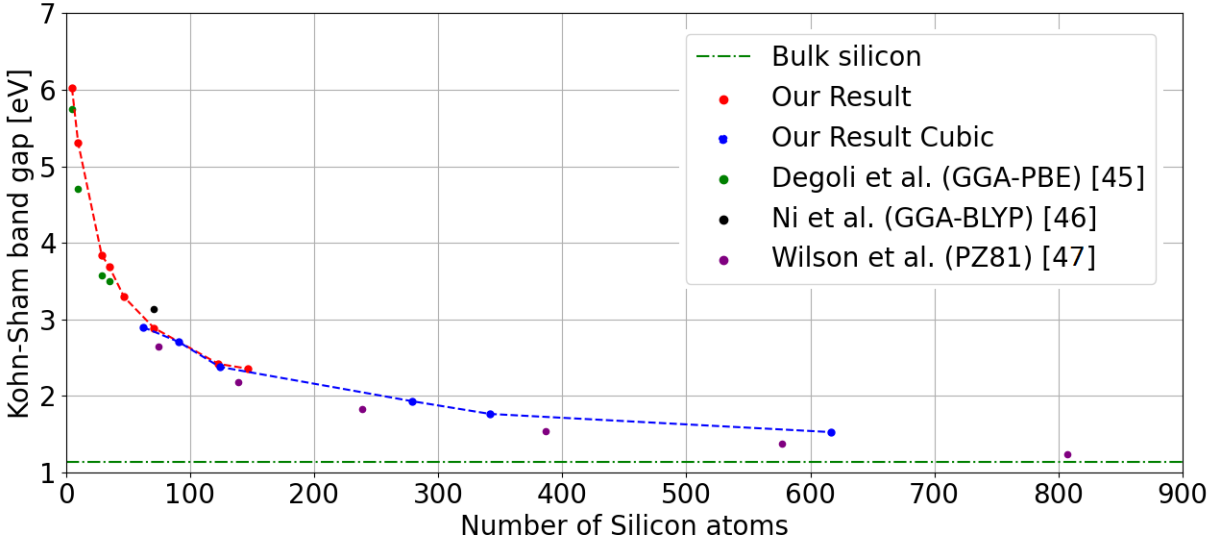


Figure 1: Results of our simulation compared to the studies mentioned above. The exchange-correlation functional type is specified in the legenda. A slight overestimation can be seen compared to most other studies.

between the HOMO and LUMO energy is an important parameter for predicting the absorptio-nal properties of a system, as it is here an approximation to the optical band-gap. A more precise band-gap can be evaluated using TDDFT. An important aspect of the HOMO-LUMO transition is the oscillator strength. It is an indication of how quickly the LUMO state decays to the HOMO state and how well the HOMO state can absorb a photon to transition to the LUMO state. The oscillator strength and derived radiative rate of this transition is relevant because most light emission happens from the LUMO to the HOMO state. This is because when an electron-hole pair is created, the electron quickly decays to the LUMO state due to phonon scattering. After this, the LUMO state transitions to the HOMO state and this is why most transitions happen between these two states when their energies are isolated from other states (see thermalized radiative rate).

5.2 Band Structures

A band structure is a graph that describes which combinations of wavenumbers and energies electrons (and holes) in a system may occupy. For an infinite crystal with long-range translational symmetry, these band structures have a well-defined energy associated with a wavenumber, k . For nanocrystals, this is not the case anymore and other methods have to be invoked to get a sense of what the band structure looks like [48]. The basic concept of this is to:

1. Solve the Kohn-Sham equations to obtain the energies and respective real-space molecular orbitals (MOs).
2. Perform a Fourier-transformation of the MOs.
3. Project MOs into the desired directions (e.g. $\Gamma - X$).
4. Plot the corresponding k-space density of states in a form of the “fuzzy” band structure.

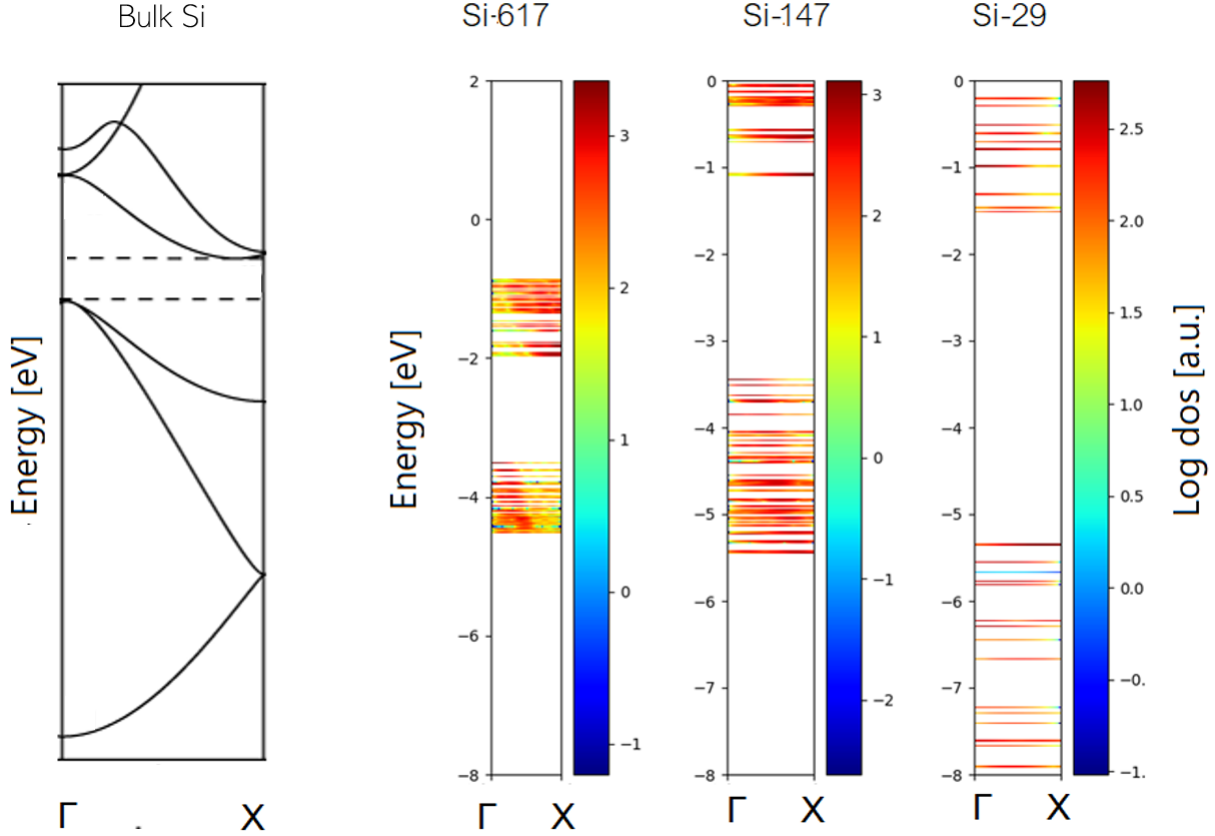


Figure 2: “Fuzzy” band structure in the Γ – X direction, displaying the effect of quantum confinement. The k -vector is less well defined in smaller Si QDs, resulting in a more direct bandgap-like transitions. On the left the bulk counterpart is displayed.

This procedure was followed first for the Si QDs coated with hydrogen and is displayed in Figure 2. It can be seen that as the nanocrystal becomes smaller, the available states get smeared out, as a result of a less well defined k -vector. On the other hand, for the larger Si QD, the indirectness of the band-gap becomes quite clear. Upon inspection in the radiative rates, however, one can see that the QDs still keep their indirect bandgap character.

5.3 Isosurface Plots Of Orbitals

An important tool for visualizing the shape of a given molecular orbital (MO) is a so-called isosurface. An isosurface can be constructed as follows:

1. Pick a non-degenerate wavefunction and make the function entries real.
2. Create a discretized space and assign values of the wavefunction to every coordinate.
3. Choose a real non-negative cutoff value between the minimum absolute value and the maximum absolute value of the wavefunction being visualized.
4. Draw a surface of constant value where the absolute value of the wave-function has the cutoff value. The boundaries of negative and positive values are often shaded in different colors.

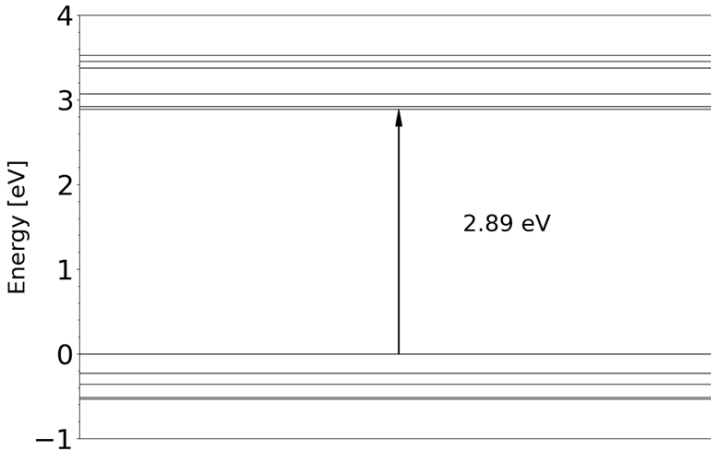


Figure 3: Energy-level diagram of the Si-71 crystal covered with hydrogen. The HOMO state and the 4 closest energy states under it are displayed as well as the LUMO state and the 4 closest states above it. The HOMO-LUMO gap is indicated by the arrow which goes from the HOMO to the LUMO state.

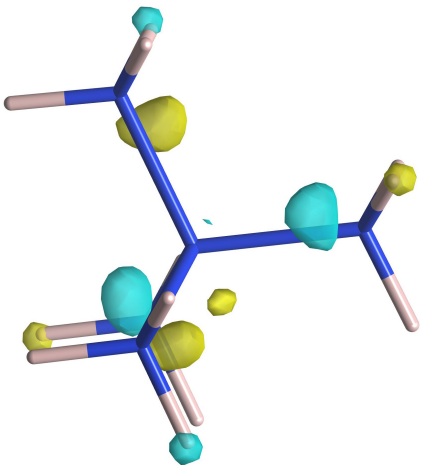
Isosurfaces are a useful tool to compare results to other DFT studies, thus making them appropriate for comparing results. Study [45] displayed multiple isosurfaces and were similar in shape to the isosurfaces obtained in our study. The main difference is the smoothness and symmetry that are not as prevalent in our isosurfaces. These differences could be explained by the fact that plane waves were used to obtain the wavefunctions. The isosurfaces as found by us and other studies for Si-5, Si-10 and Si-71 are displayed in Tables 2, 3 and 4. Although the Si-71 crystal had a very peculiar shape, our approximation still showed a similar isosurface. This also confirms the proper functioning of our simulation.

5.4 Energy-Level Diagrams

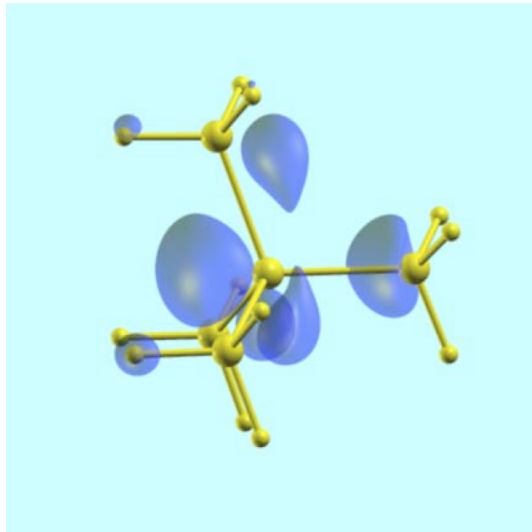
Another tool for visualizing the obtained results are energy-level diagrams. These diagrams display the available states in a system with the respective energies. The HOMO state is often set to 0 eV as a convention but this does not imply that the highest occupied state is unbound. Visualization with an energy-level diagram is useful to see the degeneracy around the bandgap. The result for Si-71 is displayed in Figure 3. The relative difference between energy levels was similar to the levels found in the study.

5.5 Thermalized Radiative Rate

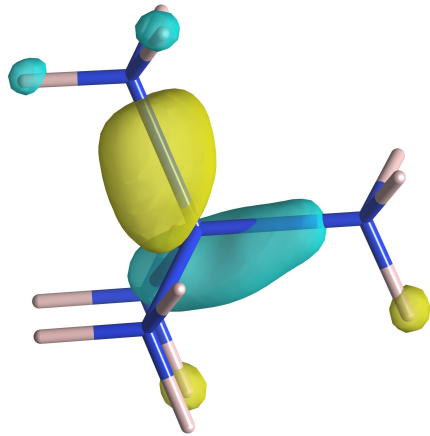
The thermalized radiative rate is an indication of how well a sample will radiate light at non-zero temperatures and is more general than the radiative rate of two states as was introduced in Equation 30. When an electron is excited by a photon, it quickly decays to the LUMO state, where it is stuck until it decays to the HOMO state. However, this is not the complete story since in real life the temperature is not zero Kelvin. A good way to take into account the effect of temperature is the Boltzmann factor. This factor is a measure for the thermal



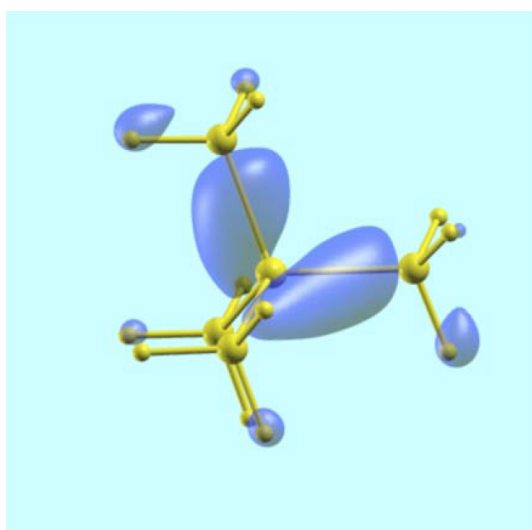
(a) LUMO state as found by us.



(b) LUMO state as found by Degoli et al.

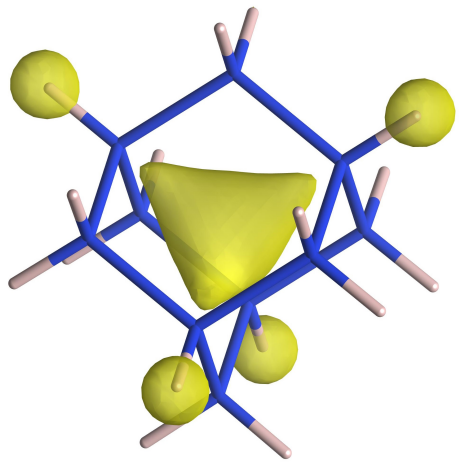


(c) HOMO state as found by us.

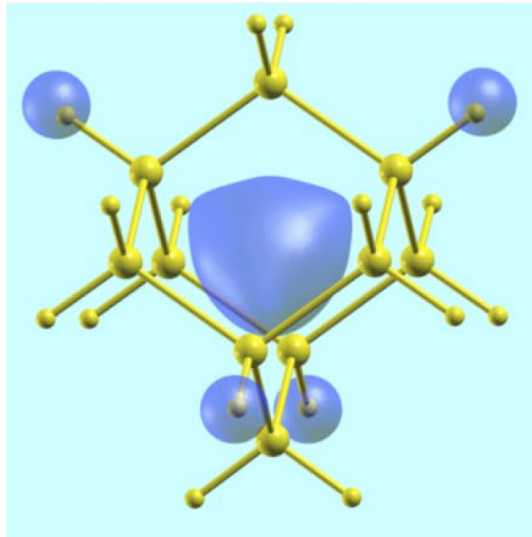


(d) HOMO state as found by Degoli et al.

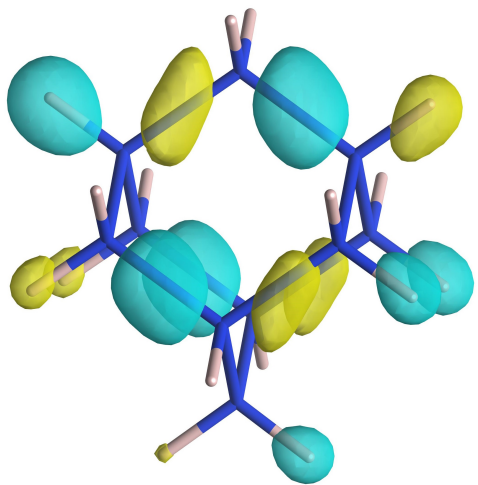
Table 2: HOMO (top) and LUMO (bottom) states of the Si-5 crystal as found by us (left) and Degoli et al. [45] (right). Isosurfaces were chosen such that the results were comparable.



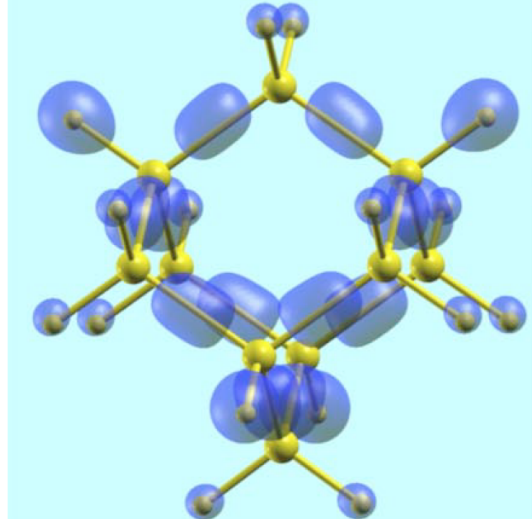
(a) LUMO state as found by us.



(b) LUMO state as found by Degoli et al.

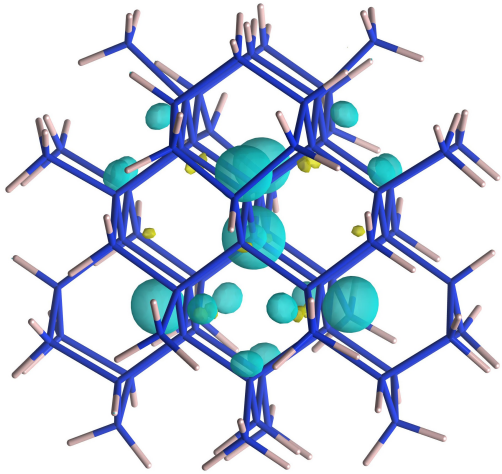


(c) HOMO state as found by us.

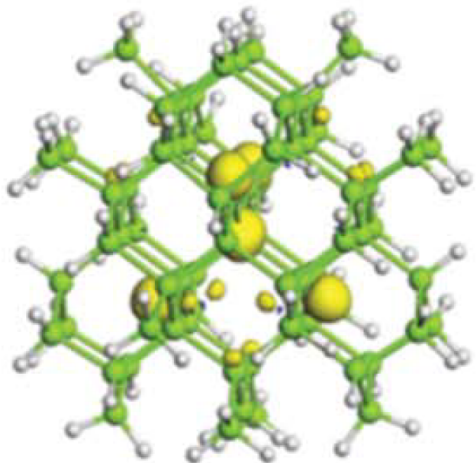


(d) HOMO state as found by Degoli et al.

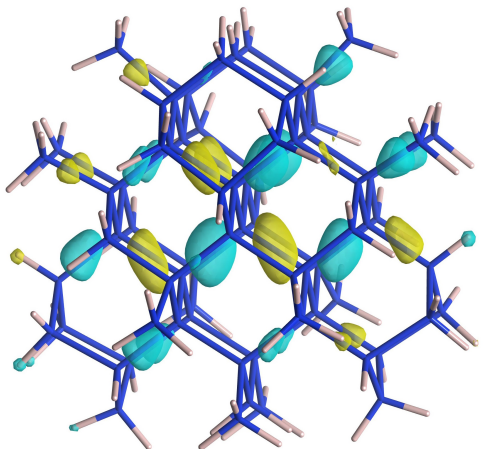
Table 3: HOMO (top) and LUMO (bottom) states of the Si-10 crystal as found by us (left) and Degoli et al. [45] (right). Isosurfaces were chosen such that the results were comparable.



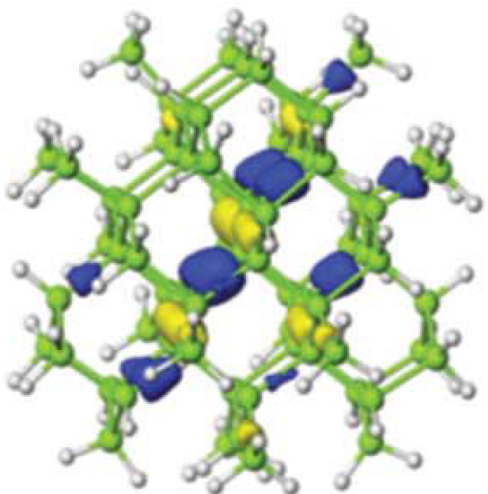
(a) LUMO state as found by us.



(b) LUMO state as found by Ni et al.



(c) HOMO state as found by us.



(d) HOMO state as found by Ni et al.

Table 4: HOMO (top) and LUMO (bottom) states of the Si-71 crystal as found by us (left) and Ni et al. [46] (right). Isosurfaces were chosen such that the results were comparable.

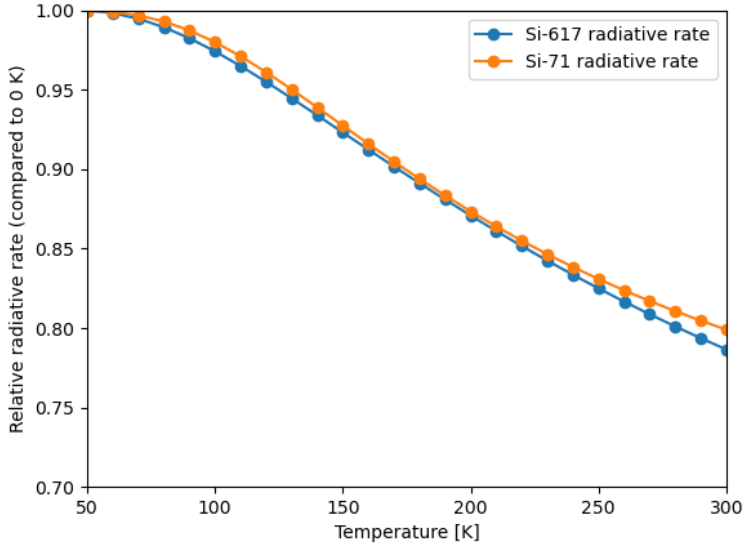


Figure 4: Relative thermalized radiative rate as a function of temperature for two simulated samples. The thermalized radiative rate decreases as a function of temperature.

energy in the sample, which has the potential to excite an electron into a higher state (in the conduction band) or to excite a hole into a lower state (in the valence band). This is done by so-called phonon-assistance, which means that the phonon donates energy to a particle so it can transition to another energy state. By using the Boltzmann factor, we essentially include the chance for the electron and hole to be in different states, which leads to a different radiative rate, namely [49]:

$$\begin{aligned} \langle k_{rad} \rangle(T) &= \frac{\sum_{i,j} k_{rad}^{ji} \exp\{-(E_{HOMO} - E_i) + (E_j - E_{LUMO})/k_b T\}}{\sum_{i,j} \exp\{-(E_{HOMO} - E_i) + (E_j - E_{LUMO})/k_b T\}} \\ &= \frac{\sum_{i,j} k_{rad}^{ji} \exp\{-E_{ji}/k_b T\}}{\sum_{i,j} \exp\{-E_{ji}/k_b T\}} \end{aligned} \quad (32)$$

The curve for two of the samples can be seen in Figure 4. We see that for both samples the thermalized radiative rate decreases as a function of temperature. From this we can conclude that higher the higher energy states for the electrons and holes have a lower radiative rate than the HOMO-LUMO gap. This is not the case for all structures, since it could also be the case that higher energy states have a higher radiative rate which would increase the thermalized radiative rate as the temperature increases.

5.6 TDDFT

To ensure the proper performance of the TDDFT, we calculated absorption spectra and excitation energies and compared them to the literature.

5.6.1 Excitation Energy

We ran calculations previously done in the literature on a Si-38 crystal [39]. The excitation energy that we found was 3.55 eV compared to the 3.41 eV that was found in the comparison study [39]. The difference can be attributed to the difference in precision basis set, or algorithms used in the code since the same exchange-correlation functional was used. Besides this result, we obtained higher excitation energies which as the energy got higher were spaced more closely. This is expected since there are more transitions in the higher energy regime.

6 Pyrene Functionalized QD

For the final simulation, we used a Si-147 sample with 2 pyrene molecules attached to the $[1,1,1]$ site. The reason for choosing this site is that it is likely the one that is most often found on real QDs (for a discussion of QD shapes see Appendix B.2). The structures as depicted in Avogadro and Vesta can be seen in Figure 5. The sample with ligands had a size of about 3.5 nm with a core diameter of 1.7 nm . Samples with long ligands attached to them take a long time to relax because the ligand has many local minima in the potential energy surface. This is also why we could not simulate many different samples because this would require an immense amount of computing power. The energy-relaxation curve of the sample can be seen in the supporting graphs (Figure 15).

6.1 HOMO- LUMO-State

The HOMO and LUMO states of the Si-147 pyrene coated QD are displayed in Figure 6. The probability density of the HOMO Kohn-Sham state is primarily located around the pyrene units and the LUMO state is located mainly in the crystal core. This can also be seen in Figure 7, where the probability density of the HOMO state is primarily focused around the carbon atoms and the LUMO state is mainly found in the silicon core.

As of now, it is unknown if this is a general property of QDs functionalized with pyrene or if this is a unique feature of this specific QD. It might be the case that upon differing the size of the QD this feature may disappear.

6.2 Charge Transfer

From Figure 6 it appears that the HOMO-LUMO transition is accompanied by a charge transfer from the ligand to the core. This charge transfer is confirmed by Figure 7, where we can see that the HOMO state is mainly focused around the ligand and the LUMO state around the core. The energy transfer from ligand to the core and subsequent decay in the core as seen in study [23] can not be explained by the HOMO and LUMO states, however, since this needs a decay from a state in the core to another state in the core. It does show that states can be centered around the pyrene units. Charge transfer has previously been linked to an increase in radiative rates of a sample [13], which will be discussed when comparing the radiative rate to the hydrogen capped QD.

6.3 Comparison To Hydrogen Capped QD

To see what the impact of the pyrene units is on the QD we compared the sample with the hydrogen capped QD, whose structure can be seen in Figure 8. The HOMO and LUMO state of

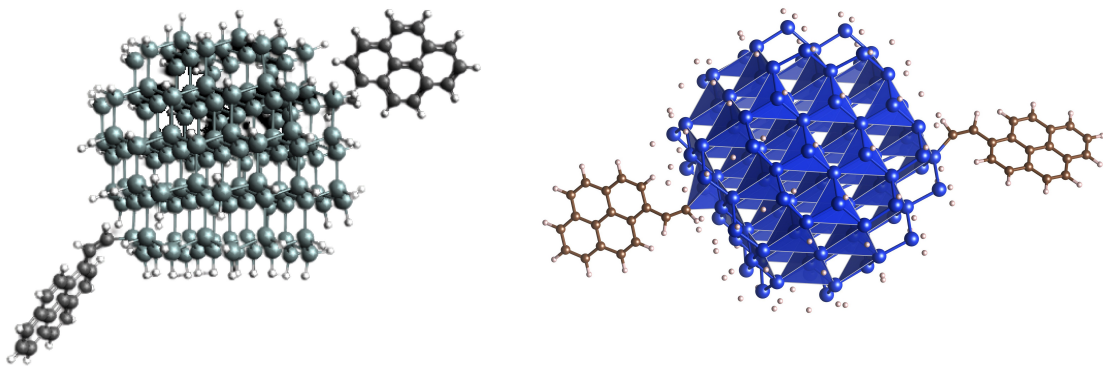


Figure 5: Structure of the pyrene functionalized Si-147 QD as depicted by Avogadro (left) and Vesta (right).

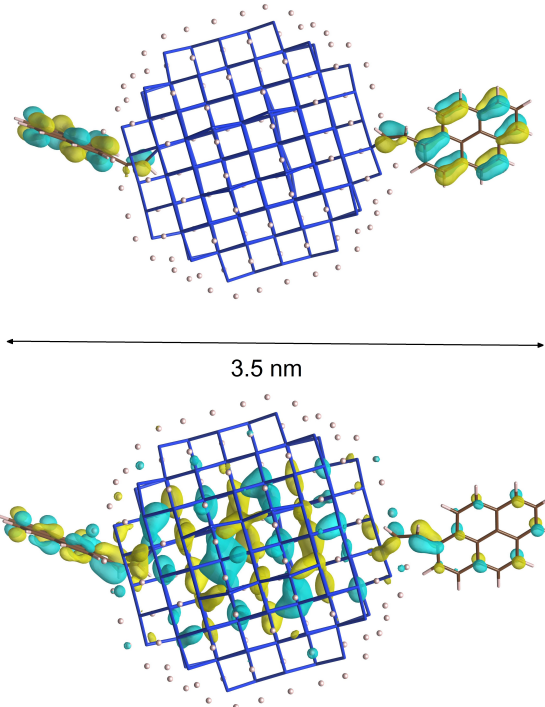


Figure 6: Isosurface plot of the Si-147 HOMO (top) and LUMO (bottom) states. The density of Kohn-Sham wavefunction of the HOMO state is found mostly around the pyrene molecules and the LUMO state is mainly found in the crystal core. The isosurface plot was chosen to have a cutoff value of 25% of the maximum value.

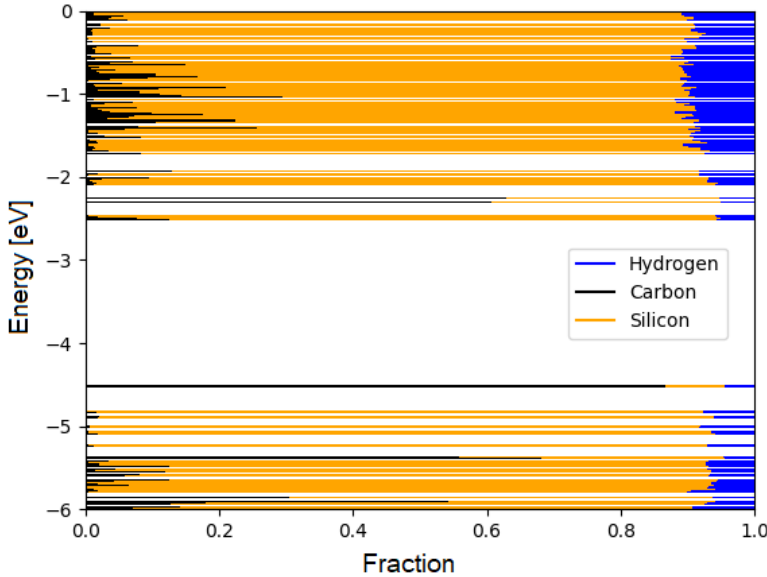


Figure 7: Energy-level diagram of the Si-147 QD with pyrene units attached to it. The x -axis indicates the fraction of the Kohn-Sham state that is centered around a type of atom. The HOMO state is primarily centered around the pyrene units and the LUMO state is primarily centered around the Si core atoms.

this sample can be seen in Figure 9. One big difference between the hydrogen capped QD and the pyrene functionalized QD is the radiative rate of states around the HOMO-LUMO transition (Figure 10). There was a significant increase for the HOMO-LUMO transition rate and an even bigger increase for higher energy transitions which can be explained by the symmetry breaking by the pyrene units. This can enhance the transition dipole moment tremendously because of the originally indirect bandgap. The difference in the radiative rate can be seen in Figure 11 (another version can be seen in the supporting info Figure 16). This figure also shows a decrease in the bandgap that is achieved in the pyrene functionalized QD. This makes intuitive sense with the particle in a box model since the carrier is less confined with the molecules attached.

6.4 Comparison Of DFT And TDDFT

To verify the DFT results, it is interesting to look at the excitation energies that are found using TDDFT. Although both DFT and TDDFT are known to underestimate the bandgap, TDDFT is better suitable for excitation energies and DFT is not. Comparing the two gives us an indication of how well the excitation energies are approximated using DFT. This comparison can be seen in Figure 12. The absorption spectrum that was found with TDDFT with Gaussian broadening as used in study [39] can be seen in Figure 13.

The Lorentzian broadening was deemed inappropriate for the spectrum of this sample since it is almost negligible. The difference in energies can be seen in the supporting information (Figure 17), which reveals that the error stays fairly constant and then triples from the 12th to 13th excitation energy. It is unknown why this divergence happens exactly at this energy, but it could be related to a different symmetry of the respective MOs.

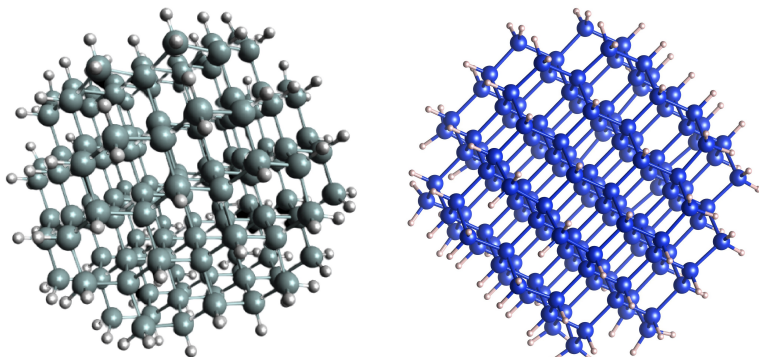


Figure 8: Structure of the hydrogen capped Si-147 QD as depicted in Avogadro (left) and Vesta (right).

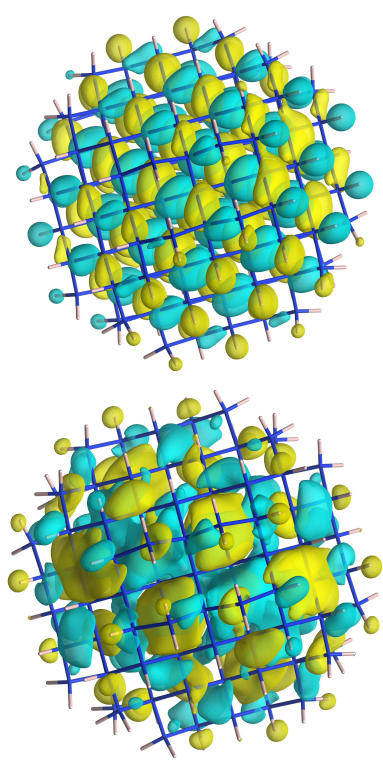


Figure 9: Isosurface plot of the Si-147 HOMO (top) and LUMO (bottom) states of the hydrogen capped QD. The cutoff value for the isosurface was chosen arbitrarily.

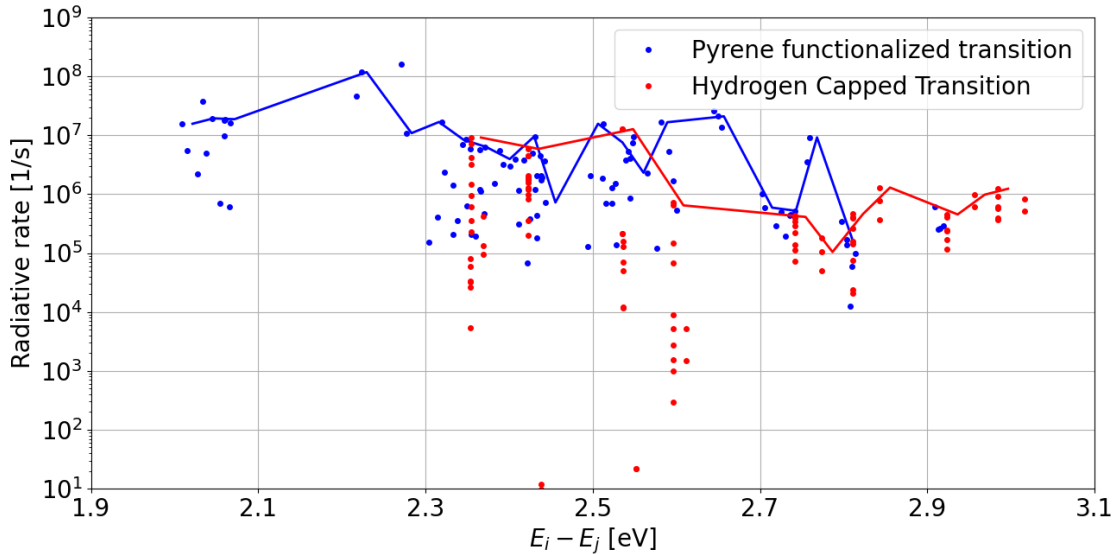


Figure 10: Radiative rate of hydrogen capped and pyrene functionalized QD. There is a significant increase in the radiative rate when the QD has pyrene units attached to it in some regimes. It can also be seen that the bandgap has decreased with this functionalization.

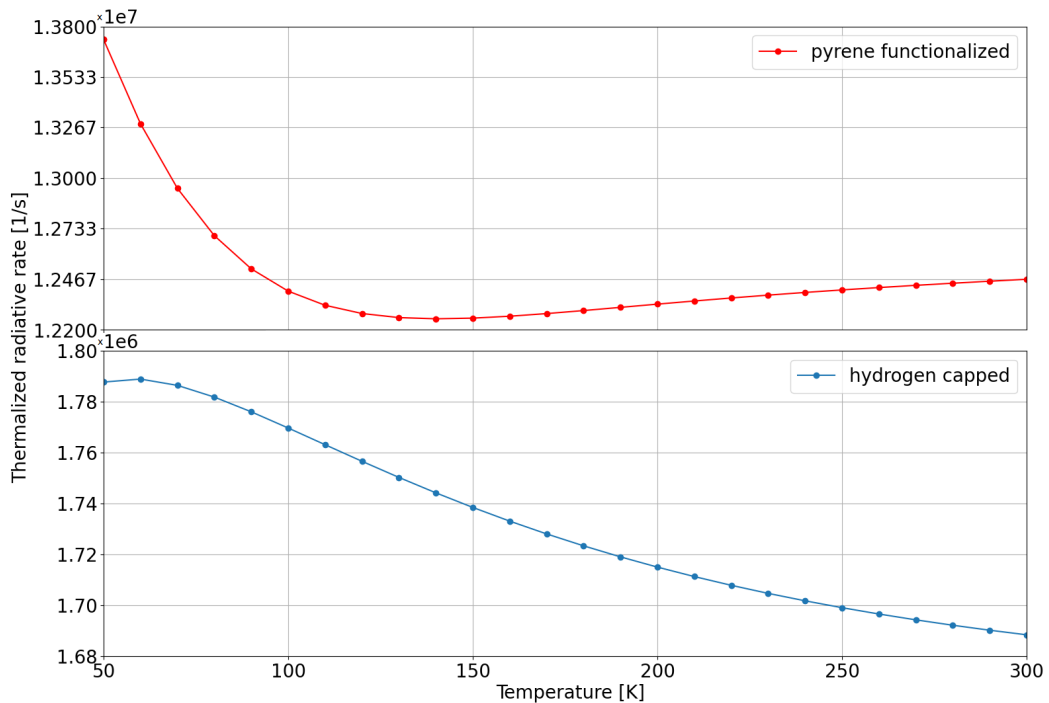


Figure 11: Thermalized radiative rate as introduced in equation 32 of hydrogen capped and pyrene functionalized QD as a function of temperature. There is a significant increase in the radiative rate when the QD is functionalized, but also a relatively big decrease at higher temperatures as compared to the hydrogen capped QD.

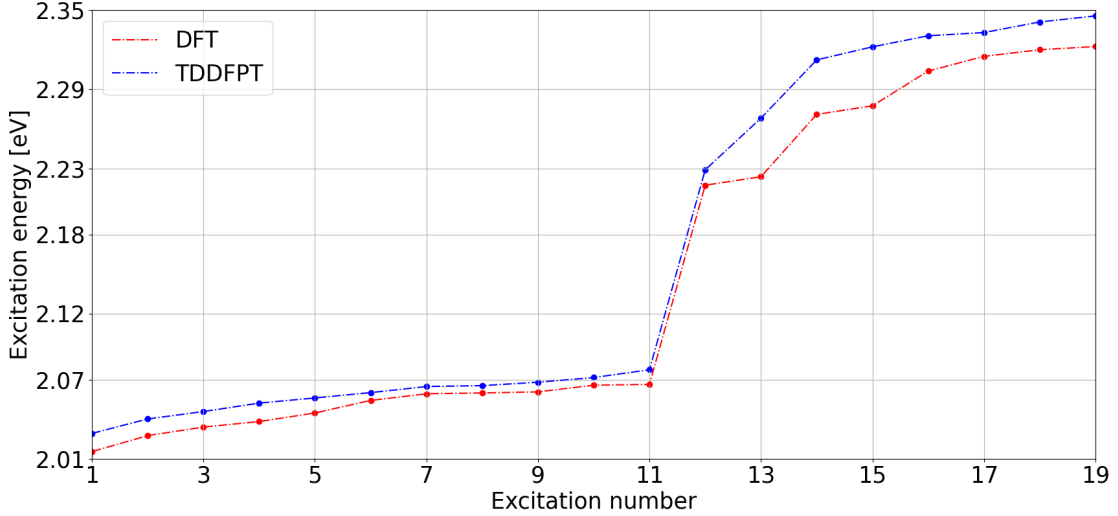


Figure 12: Comparison between the excitation energies found with DFT and TDDFT. The excitation number indicates which excitation mode is represented. The bandgap corresponds to excitation number 1 and the second to lowest excitation energy corresponds to excitation number 2 etc.

We also compared the radiative rates found with DFT and TDDFT (Figure 14). The DFT generally had a higher rate than the TDDFT calculation. There could be a mismatch between excitation numbers of the DFT and TDDFT excitation modes which would explain the mismatch, but this is unexpected since the excitation energies match so well.

6.5 Comparison To Experiment

The structure we studied was also synthesized in Ref. [23]. Although the size of the silicon QD particles in this study varied greatly it was found that the emission lifetime (which can be interpreted as $1/\langle k_{rad} \rangle$) of pyrene functionalized QD decreased as compared to the pyrene indicating that the FRET mechanism is at play. This is comparable to the charge transfer we found from the pyrene to the QD which would also reduce the lifetime of the pyrene excitation. The experiment, unfortunately, did not look at the difference in the luminescence of the pyrene functionalized sample and the hydrogen capped counterpart, making it hard to compare the difference in thermalized radiative rates we found in the simulation.

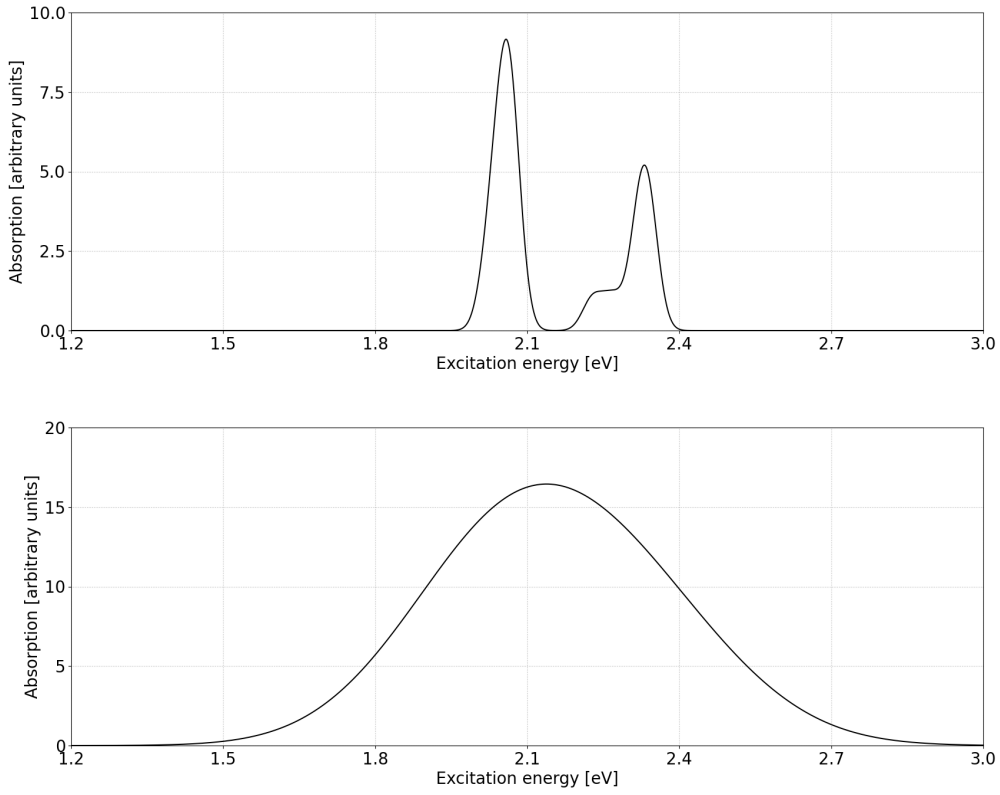


Figure 13: Spectrum produced by the first 20 excitation modes of the pyrene functionalized QD as calculated by TDDFT. Gaussian broadening with a standard deviation of 20 meV (top) and 200 meV (bottom) were used to broaden the delta-peaks.

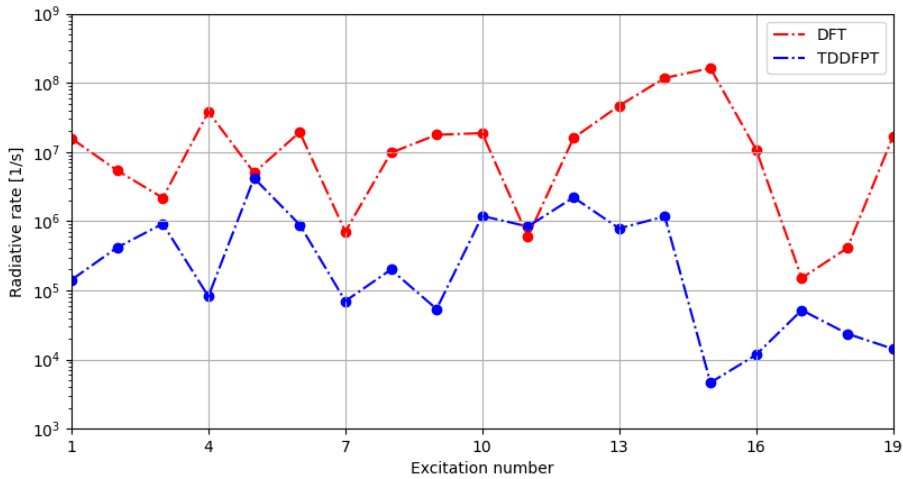


Figure 14: Comparison between the radiative rates found with DFT and TDDFT. The excitation number indicates which excitation mode is represented. The bandgap corresponds to excitation number 1 and the second to lowest excitation energy corresponds to excitation number 2 etc. Note that this is not the thermalized radiative rate.

7 Discussion And Outlook

This project revealed that radiative rates of silicon QDs can be enhanced and significant charge transfer can be induced when functionalized with the right molecules. The results align themselves with previous theoretical research of surface modification, but it was not possible to compare the results to the experiment.

One factor this investigation did not take into account was the size of the silicon QD, which may have a big impact since the efficiency of the FRET mechanism depends on the excitation energy of the donor as well as the acceptor. We suspect that there is an optimal excitation energy for the QD, where the radiative rate is the highest which alters per attached molecule.

Some molecules that might be interesting to simulate or experiment with are 1-Pyrenemethyl methacrylate, (10-Methylanthracen-9-YL) methyl 2-methylprop-2-enoate and 1-Naphthylmethyl vinyl ether. Numerous molecules have the potential to tremendously increase the radiative rate of the QD. Besides other ligands, there is also the possibility to attach oxygen or nitrogen molecules to the pyrene molecule, which increases the asymmetry of the structure, which in turn, could increase the radiative rate or change the emission and absorption spectrum [50].

8 Conclusion

The main result is an increase in the radiative rates with the functionalization of pyrene. This was caused by the breaking of the symmetry of the Si QD by surface functionalization and the co-localization of the electronic states on the ligand. Besides this, we discovered a possible charge transfer from the ligand to the core upon certain excitations.

Using DFT it was possible to predict the radiative rates and other parameters from first principles and when we compared the DFT results to the TDDFT results we found that the excitation energies agreed, but the radiative rates disagreed.

The next step is to calculate other sorts of functionalizations of Si QDs to find molecules that enhance the properties of the Si QD even more to make the QDs more practically applicable. Furthermore, it should be investigated how the radiative rate depends on the QD size.

9 Acknowledgments

I would like to thank my supervisor Katerina Dohnalova for helping me out tremendously with this bachelor thesis. She was often available at weekends and always glad to explain crucial concepts to me. It was a pleasure to do my thesis at the WZI and the group meetings were always entertaining. Besides her, I would like to thank Morice Corentin for answering my technical questions about density functional theory. Without them, I would have been stuck continually.

A Installing CP2K On Linux

A.1 Installation

This section will provide a small manual on how to install an older version on CP2K. This version of CP2K misses some features like TDDFT but can perform more basic calculations. Synaptic is a package manager for Linux which will be used here. The program is installed by opening the terminal and executing the following command:

```
sudo apt-get install synaptic
```

Once the installation is done we open synaptic, select the search button, and input CP2K as a search term. We mark CP2K for installation which will notify us that the CP2K-data package also has to be installed for CP2K to work. We select the mark option and both packages are now marked for installation. After this, we click the apply button. Make sure that CP2K and CP2K data are under the "To be installed" header. Press apply and wait for the packages to install. To see whether or not the installation was successful we execute the following command:

```
cp2k
```

This should give us an output of how the program should be executed.

A.2 Execution

Now that we are ready to use CP2K we can take a look at what the typical project structure looks like and how to execute it. For a typical CP2K simulation 5 files are required at most:

1. CP2K input file
2. Basis set file
3. Potential file
4. Coordinate file of the simulated system
5. Job file

The composition of the input file can be found in the CP2K manual. It is also helpful to look at examples that are listed online. An appropriate basis set and (pseudo)potential then have to be picked. For most calculations the MOLOPT basis set and the GTH pseudopotentials are appropriate, but this depends on what is desired from the simulation. The files for this basis set and pseudopotential can be found on the CP2K GitHub repository. The last two files are optional. A coordinate file can be used to specify the (initial) atomic positions which can be convenient when designing systems in Avogadro or Vesta. For CP2K to find this file, we need to specify the filename as follows in the TOPOLOGY section of the CP2K input file. The last file that can be used is a job file, but this is only necessary when performing calculations on clusters. This file specifies the time, nodes, and modules that are needed from the cluster to perform the calculation.

Once the files are placed in a directory, navigate the terminal to this directory by executing the change directory command:

```
cd folder_with_files
```

Once we are in this directory, we start the simulation by the following command:

```
cp2k.popt -i inputFileName -o outputFileName
```

In this example, we are using the parallel version of CP2K, but there is also a sequentially optimized version (cp2k.sopt). When we are using a cluster we can submit the job file by being in the directory with the required files and typing:

```
sbatch JobFileName
```

After submitting or starting the calculation the output file will append all the relevant information.

B Supporting information

Some graphs and sections were not relevant enough to put in the report but are worth mentioning are discussed in this section.

B.1 Supporting Graphs

First of all, we have a graph of the relative radiative rate as compared to the H-capped QD at $T = 0\text{ K}$ in Figure 16. This graph can give a quick view of how much the thermalized radiative rate increases when the QD is functionalized. In Figure 17 we can see the difference in excitation energies of the DFT and TDDFT calculation. There is a significant increase of error at higher energies. The cause for this divergence is unknown. When relaxing the pyrene functionalized structure we checked that it did so properly by looking at the energy convergence graph. The energy convergence of the sample can be seen in 15. Here the total energy of the system is displayed as a function of the number of steps taken. It is clear from the smoothness of this figure that the system converged properly.

B.2 Shape Of Realistic QDs

To investigate what the most stable form of QDs is, we tried investigating the surface binding energies of the different miller planes of QDs. This gives us an indication of what kind of plane is energetically preferred. To investigate the surface energy we used the QD that will later be used to calculate properties with ligands, which is the Si-147 QD. We took a simple approach for deciding which structure is most stable by looking at the $\text{Si}_3\text{-H}$, $\text{Si}_2\text{-H}_2$ and $\text{Si}\text{-H}_3$ surfaces. Since Si-Si bonds are the only bonds that contribute to the binding to the crystal we can conclude that the surface with the most Si-Si bonds and hence the planes that only have one hydrogen attached to them are the most stable. The planes with more hydrogens would be more prone to reacting with the environment and hence they are the most unstable surfaces.

Recently, a paper was released that investigated the strain of Pt nanoparticles, revealing that nanoparticles tend to have a positive strain [51]. Our relaxed structures revealed similar properties but deviated in the fact that the strain decreased with radial distance as opposed to staying constant (Figure 18, 19). This is another verification for the proper relaxation of the structure.

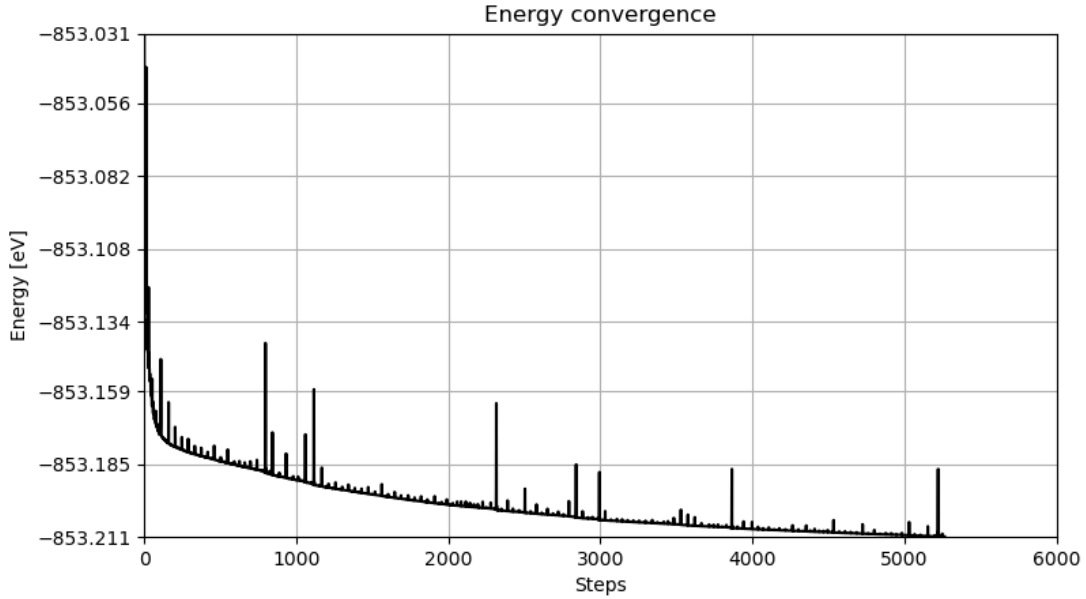


Figure 15: The total energy of the sample as a function of the number of iterations. It can be seen that the sample progresses towards an energy minimum as expected. The sample took around 5000 steps to relax.

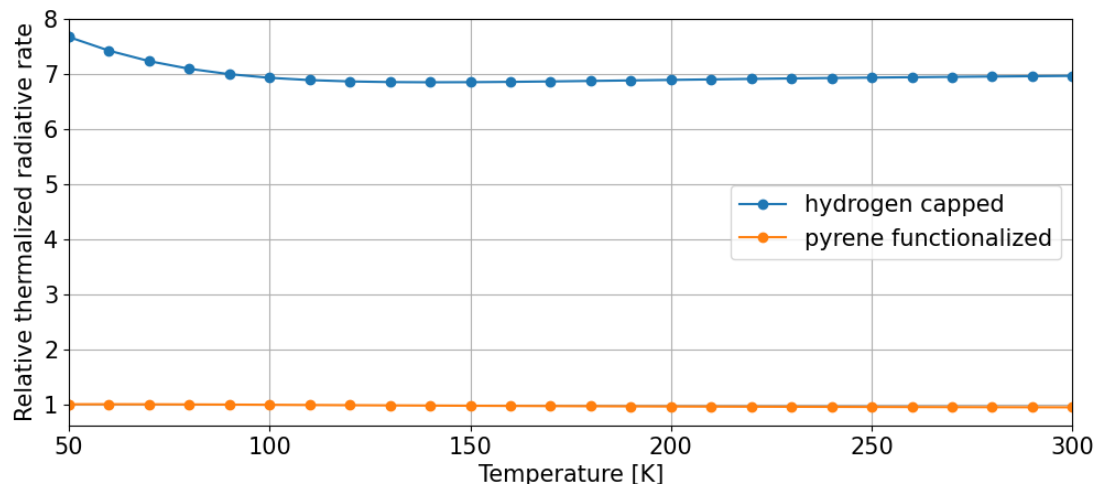


Figure 16: Relative thermalized radiative rate as introduced in equation 32 of hydrogen capped and pyrene functionalized QD as compared to hydrogen capped at 0 K as a function of temperature. There is a significant increase in the radiative rate when the QD is functionalized, but also a relatively big decrease at higher temperatures as compared to the hydrogen capped QD.

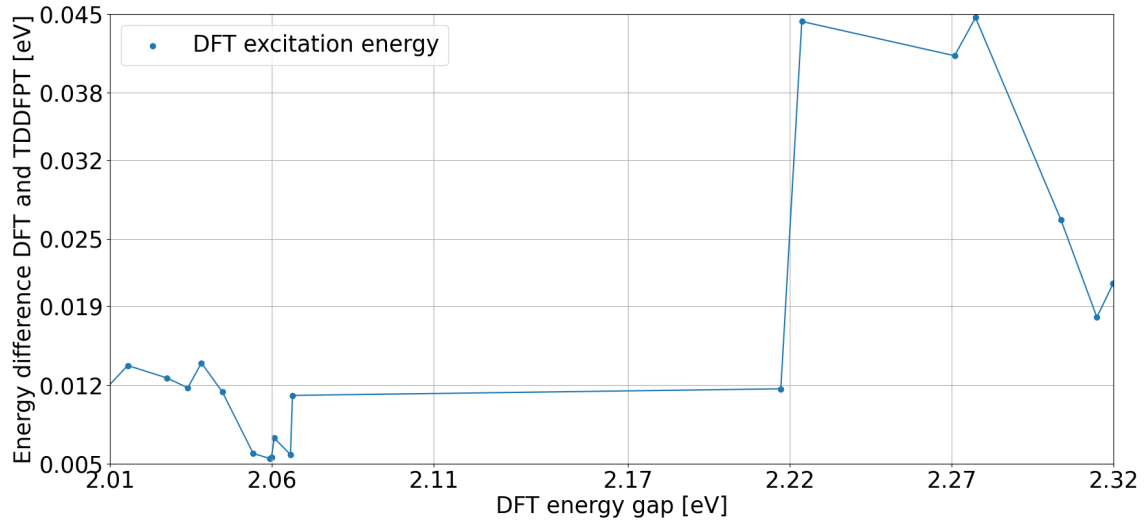


Figure 17: Difference in excitation energy between DFT and TDDFT as a function of DFT excitation energies. There is a significant increase in the difference at the 13-th excitation energy.

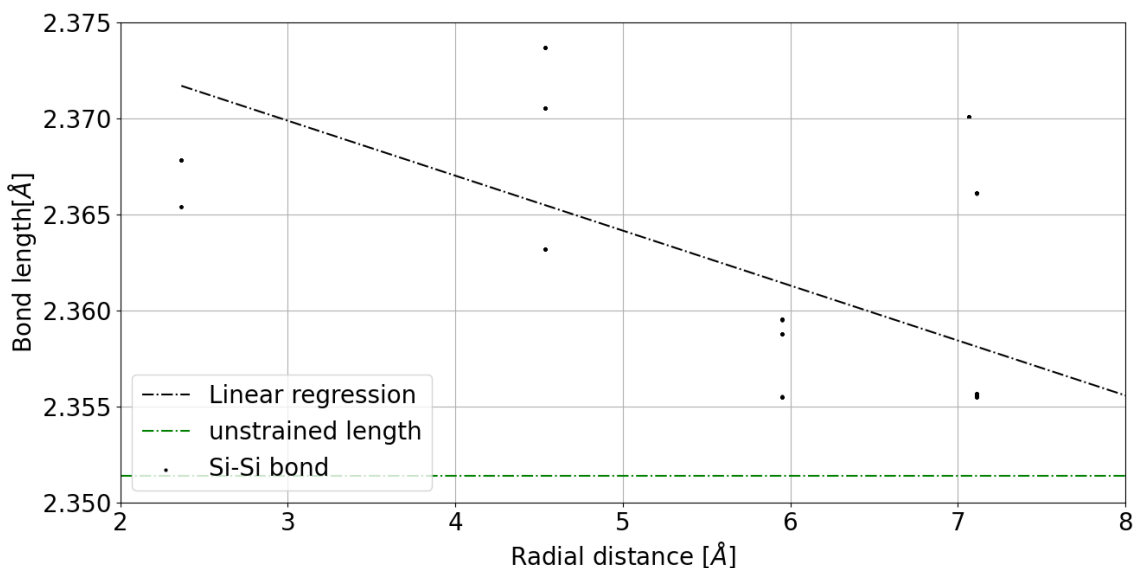


Figure 18: Radial dependence of the Si-Si bonds within the Si-147 nanocrystal. Most bonds are stretched out compared to the bond length in bulk silicon.

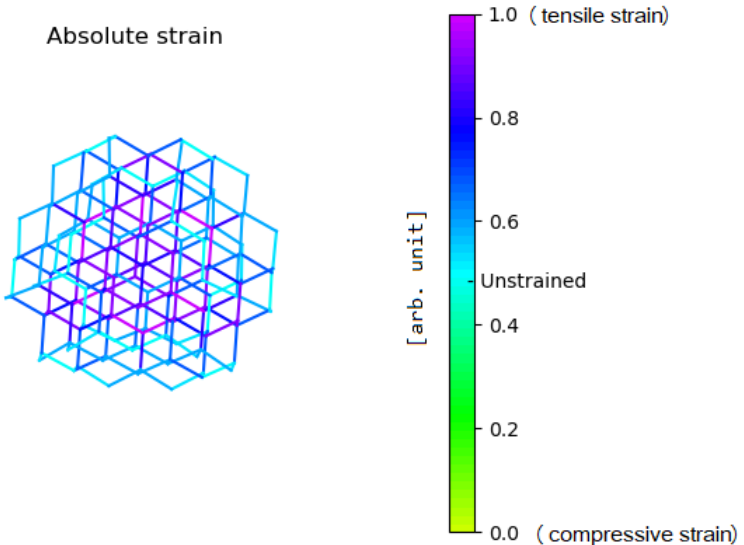


Figure 19: Lengths of the Si-Si bonds in the Si-147 crystal. The bonds around the crystal center are stretched out most, compared to the other bonds.

References

- [1] D. L. Anderson, *Theory of the Earth*. Blackwell scientific publications, 1989.
- [2] J. Ebenezar, “Recent trends in materials science and applications,” *Springer Proceedings in Physics*, vol. 189, p. 396, 2017.
- [3] C. B. Murray, a. C. Kagan, and M. Bawendi, “Synthesis and characterization of monodisperse nanocrystals and close-packed nanocrystal assemblies,” *Annual review of materials science*, vol. 30, no. 1, pp. 545–610, 2000.
- [4] L. Mangolini, E. Thimsen, and U. Kortshagen, “High-yield plasma synthesis of luminescent silicon nanocrystals,” *Nano letters*, vol. 5, no. 4, pp. 655–659, 2005.
- [5] J. A. Kelly, E. J. Henderson, and J. G. Veinot, “Sol-gel precursors for group 14 nanocrystals,” *Chemical communications*, vol. 46, no. 46, pp. 8704–8718, 2010.
- [6] M. Wolkin, J. Jorne, P. Fauchet, G. Allan, and C. Delerue, “Electronic states and luminescence in porous silicon quantum dots: the role of oxygen,” *Physical Review Letters*, vol. 82, no. 1, p. 197, 1999.
- [7] A. Goyal and P. Soni, “Functionally graded nanocrystalline silicon powders by mechanical alloying,” *Materials Letters*, vol. 214, pp. 111–114, 2018.
- [8] E. Jang, S. Jun, H. Jang, J. Lim, B. Kim, and Y. Kim, “White-light-emitting diodes with quantum dot color converters for display backlights,” *Advanced materials*, vol. 22, no. 28, pp. 3076–3080, 2010.

- [9] K. Dohnalová, T. Gregorkiewicz, and K. Ksová, “Silicon quantum dots: surface matters,” *Journal of Physics: Condensed Matter*, vol. 26, no. 17, p. 173201, 2014.
- [10] M. A. Walling, J. A. Novak, and J. R. Shepard, “Quantum dots for live cell and in vivo imaging,” *International journal of molecular sciences*, vol. 10, no. 2, pp. 441–491, 2009.
- [11] C. T. Matea, T. Mocan, F. Tabaran, T. Pop, O. Mosteanu, C. Puia, C. Iancu, and L. Mocan, “Quantum dots in imaging, drug delivery and sensor applications,” *International journal of nanomedicine*, vol. 12, p. 5421, 2017.
- [12] H. Yamada and N. Shirahata, “Silicon quantum dot light emitting diode at 620 nm,” *Micromachines*, vol. 10, no. 5, p. 318, 2019.
- [13] A. Poddubny and K. Dohnalová, “Direct band gap silicon quantum dots achieved via electronegative capping,” *Physical Review B*, vol. 90, no. 24, p. 245439, 2014.
- [14] K. Ksová, P. Hapala, J. Valenta, P. Jelínek, O. Cibulka, L. Ondič, and I. Pelant, “Direct bandgap silicon: Tensile-strained silicon nanocrystals,” *Advanced Materials Interfaces*, vol. 1, no. 2, p. 1300042, 2014.
- [15] J. D. Holmes, K. J. Ziegler, R. C. Doty, L. E. Pell, K. P. Johnston, and B. A. Korgel, “Highly luminescent silicon nanocrystals with discrete optical transitions,” *Journal of the American Chemical Society*, vol. 123, no. 16, pp. 3743–3748, 2001.
- [16] M. Dasog, G. B. De los Reyes, L. V. Titova, F. A. Hegmann, and J. G. Veinot, “Size vs surface: tuning the photoluminescence of freestanding silicon nanocrystals across the visible spectrum via surface groups,” *ACS nano*, vol. 8, no. 9, pp. 9636–9648, 2014.
- [17] A. Fermi, M. Locritani, G. Di Carlo, M. Pizzotti, S. Caramori, Y. Yu, B. A. Korgel, G. Bergamini, and P. Ceroni, “Light-harvesting antennae based on photoactive silicon nanocrystals functionalized with porphyrin chromophores,” *Faraday discussions*, vol. 185, pp. 481–495, 2015.
- [18] M. Locritani, Y. Yu, G. Bergamini, M. Baroncini, J. K. Molloy, B. A. Korgel, and P. Ceroni, “Silicon nanocrystals functionalized with pyrene units: efficient light-harvesting antennae with bright near-infrared emission,” *The journal of physical chemistry letters*, vol. 5, no. 19, pp. 3325–3329, 2014.
- [19] A. Sommer, C. Cimpean, M. Kunz, C. Oelsner, H. J. Kupka, and C. Kryschi, “Ultrafast excitation energy transfer in vinylpyridine terminated silicon quantum dots,” *The Journal of Physical Chemistry C*, vol. 115, no. 46, pp. 22781–22788, 2011.
- [20] M. Rosso-Vasic, E. Spruijt, B. Van Lagen, L. De Cola, and H. Zuilhof, “Alkyl-functionalized oxide-free silicon nanoparticles: Synthesis and optical properties,” *Small*, vol. 4, no. 10, pp. 1835–1841, 2008.
- [21] F. Romano, Y. Yu, B. A. Korgel, G. Bergamini, and P. Ceroni, “Light-harvesting antennae based on silicon nanocrystals,” in *Photoactive Semiconductor Nanocrystal Quantum Dots*, pp. 89–106, Springer, 2017.

- [22] Y. Li, W. Li, H. Zhang, Y. Liu, L. Ma, and B. Lei, “Amplified light harvesting for enhancing italien lettuce photosynthesis using water soluble silicon quantum dots as artificial antennas,” *Nanoscale*, vol. 12, no. 1, pp. 155–166, 2020.
- [23] M. Abdelhameed, D. R. Martir, S. Chen, W. Z. Xu, O. O. Oyeneye, S. Chakrabarti, E. Zysman-Colman, and P. A. Charpentier, “Tuning the optical properties of silicon quantum dots via surface functionalization with conjugated aromatic fluorophores,” *Scientific reports*, vol. 8, no. 1, pp. 1–10, 2018.
- [24] A. R. Clapp, I. L. Medintz, and H. Mattoussi, “Förster resonance energy transfer investigations using quantum-dot fluorophores,” *ChemPhysChem*, vol. 7, no. 1, pp. 47–57, 2006.
- [25] J. L. Wilbrink, C.-C. Huang, K. Dohnalova, and J. M. Paulusse, “Critical assessment of wet-chemical oxidation synthesis of silicon quantum dots,” *Faraday Discussions*, 2020.
- [26] P. Hohenberg and W. Kohn, “Inhomogeneous electron gas physical review 136,” *B864*, 1964.
- [27] W. Kohn and L. J. Sham, “Self-consistent equations including exchange and correlation effects,” *Physical review*, vol. 140, no. 4A, p. A1133, 1965.
- [28] E. Baerends, O. Gritsenko, and R. Van Meer, “The kohn–sham gap, the fundamental gap and the optical gap: the physical meaning of occupied and virtual kohn–sham orbital energies,” *Physical Chemistry Chemical Physics*, vol. 15, no. 39, pp. 16408–16425, 2013.
- [29] S. F. Sousa, P. A. Fernandes, and M. J. Ramos, “General performance of density functionals,” *The Journal of Physical Chemistry A*, vol. 111, no. 42, pp. 10439–10452, 2007.
- [30] L. Lin and J. Lu, *A Mathematical Introduction to Electronic Structure Theory*. SIAM, 2019.
- [31] P. A. Dirac, “Note on exchange phenomena in the thomas atom,” in *Mathematical Proceedings of the Cambridge Philosophical Society*, vol. 26, pp. 376–385, Cambridge University Press, 1930.
- [32] F. Giustino, *Materials modelling using density functional theory: properties and predictions*. Oxford University Press, 2014.
- [33] S. Huzinaga, “Basis sets for molecular calculations,” *Computer physics reports*, vol. 2, no. 6, pp. 281–339, 1985.
- [34] J. VandeVondele, M. Krack, F. Mohamed, M. Parrinello, T. Chassaing, and J. Hutter, “Quickstep: Fast and accurate density functional calculations using a mixed gaussian and plane waves approach,” *Computer Physics Communications*, vol. 167, no. 2, pp. 103–128, 2005.
- [35] V. Peuckert, “A new approximation method for electron systems,” *Journal of Physics C: Solid State Physics*, vol. 11, no. 24, p. 4945, 1978.
- [36] E. Runge and E. K. Gross, “Density-functional theory for time-dependent systems,” *Physical Review Letters*, vol. 52, no. 12, p. 997, 1984.

- [37] R. van Leeuwen, “Mapping from densities to potentials in time-dependent density-functional theory,” *Physical review letters*, vol. 82, no. 19, p. 3863, 1999.
- [38] W. Demtröder, *Laser spectroscopy: basic concepts and instrumentation*. Springer Science & Business Media, 2013.
- [39] R. Derian, K. Tokár, B. Somogyi, Á. Gali, and I. Stich, “Optical gaps in pristine and heavily doped silicon nanocrystals: Dft versus quantum monte carlo benchmarks,” *Journal of chemical theory and computation*, vol. 13, no. 12, pp. 6061–6067, 2017.
- [40] K. Momma and F. Izumi, “Vesta 3 for three-dimensional visualization of crystal, volumetric and morphology data,” *Journal of applied crystallography*, vol. 44, no. 6, pp. 1272–1276, 2011.
- [41] M. D. Hanwell, D. E. Curtis, D. C. Lonie, T. Vandermeersch, E. Zurek, and G. R. Hutchison, “Avogadro: an advanced semantic chemical editor, visualization, and analysis platform,” *Journal of cheminformatics*, vol. 4, no. 1, p. 17, 2012.
- [42] J. VandeVondele and J. Hutter, “Gaussian basis sets for accurate calculations on molecular systems in gas and condensed phases,” *The Journal of chemical physics*, vol. 127, no. 11, p. 114105, 2007.
- [43] S. Goedecker, M. Teter, and J. Hutter, “Separable dual-space gaussian pseudopotentials,” *Physical Review B*, vol. 54, no. 3, p. 1703, 1996.
- [44] J. P. Perdew, K. Burke, and M. Ernzerhof, “Generalized gradient approximation made simple,” *Physical review letters*, vol. 77, no. 18, p. 3865, 1996.
- [45] E. Degoli, G. Cantele, E. Luppi, R. Magri, D. Ninno, O. Bisi, and S. Ossicini, “Ab initio structural and electronic properties of hydrogenated silicon nanoclusters in the ground and excited state,” *Physical Review B*, vol. 69, no. 15, p. 155411, 2004.
- [46] Z. Ni, X. Pi, and D. Yang, “Density functional theory study on a 1.4 nm silicon nanocrystal coated with carbon,” *RSC advances*, vol. 2, no. 30, pp. 11227–11230, 2012.
- [47] H. F. Wilson, L. McKenzie-Sell, and A. S. Barnard, “Shape dependence of the band gaps in luminescent silicon quantum dots,” *Journal of Materials Chemistry C*, vol. 2, no. 44, pp. 9451–9456, 2014.
- [48] P. Hapala, K. Ksová, I. Pelant, and P. Jelínek, “Theoretical analysis of electronic band structure of 2-to 3-nm si nanocrystals,” *Physical Review B*, vol. 87, no. 19, p. 195420, 2013.
- [49] K. Dohnalova, P. Hapala, K. Ksová, and I. Infante, “Electronic structure engineering achieved via organic ligands in silicon nanocrystals,” *Chemistry of Materials*, 2020.
- [50] B. van Dam, H. Nie, B. Ju, E. Marino, J. M. Paulusse, P. Schall, M. Li, and K. Dohnalová, “Excitation-dependent photoluminescence from single-carbon dots,” *Small*, vol. 13, no. 48, p. 1702098, 2017.
- [51] B. H. Kim, J. Heo, S. Kim, C. F. Reboul, H. Chun, D. Kang, H. Bae, H. Hyun, J. Lim, H. Lee, *et al.*, “Critical differences in 3d atomic structure of individual ligand-protected nanocrystals in solution,” *Science*, vol. 368, no. 6486, pp. 60–67, 2020.